FEDERAL UNIVERSITY OF RIO GRANDE DO SUL
INSTITUTE OF PHYSICS, DEPARTMENT OF PHYSICS
GRADUATE PROGRAM IN PHYSICS

Lucas Doria de Carvalho

Analysis of the mean transverse momentum as a function of charged-particle multiplicity in proton-lead collisions at 5.02 TeV and 8.16 TeV using the CMS detector at the LHC

Porto Alegre
2026

Lucas Doria de Carvalho

Analysis of the mean transverse momentum as a function of charged-particle multiplicity in proton-lead collisions at 5.02 TeV and 8.16 TeV using the CMS detector at the LHC

Original version

Dissertation submitted to the Graduate Program in Physics of the Federal University of Rio Grande do Sul (UFRGS) as a partial requirement for the degree of Master of Science in Physics.

Area of concentration: Heavy-Ion Collisions, Data Analysis, Quark–Gluon Plasma.

Corrected version incorporating the revisions requested by the examination committee. Porto Alegre, 13 February 2026.

Advisor: Dr. César Augusto Bernardes

Porto Alegre

2026

Ficha catalográfica

Dissertation authored by Lucas Doria de Carvalho, entitled **"Analysis of the mean transverse momentum as a function of charged-particle multiplicity in proton-lead collisions at 5.02 TeV and 8.16 TeV using the CMS detector at the LHC"**, submitted to the Department of Physics of the Federal University of Rio Grande do Sul in partial fulfillment of the requirements for the degree of Master of Science in Physics in the Graduate Program in Physics, in the area of Experimental Physics, approved on 13 February 2026 by the examining committee composed of the following Ph.D. members:

Ph.D. César Augusto Bernardes

São Paulo State University (UNESP)

President

Ph.D. Gustavo Gil da Silveira

Federal University of Rio Grande do Sul (UFRGS)

Ph.D. Magno Machado

Federal University of Rio Grande do Sul (UFRGS)

Ph.D. Fernando Gardim

Federal University of Alfenas

Acknowledgements

I would like to express my sincere gratitude to:

- My advisor, Prof. Dr. César Augusto Bernardes, for the productive discussions, scientific guidance, patience and continuous support throughout during the development of this project.

- The members of the examining committee for their valuable comments and suggestions.

- My collaborators and colleagues from the SPRACE and GASP-IF/UFRGS for providing an excelent scientific environment in which this project was be developed.

- The faculty and staff of the Graduate Program in Physics from UFRGS for administrative and academic support.

- The funding agency Conselho Nacional de Desenvolvimento Científico e Tecnológico (CNPq) which financially supported this work, making this research possible.

- My family for their unconditional support throughout my academic journey. In particular, I am grateful for my parents, my father and my mother, for their trust and for all the emotional and personal support I received.

Resumo

Colisões de íons pesados ultrarrelativísticas criam um volume substancial de um estado desconfinado de matéria de curta duração conhecido como plasma de quarks e glúons (QGP). Além disso, experimentos realizados no Relativistic Heavy Ion Collider (RHIC) e no Large Hadron Collider (LHC) demonstraram que o QGP produzido em colisões de íons pesados de alta energia se comporta como um fluido quase perfeito fortemente acoplado. O comportamento coletivo em sistemas de colisão pode ser estudado por meio da análise da correlação entre o momento transversal médio $\langle p_{\mathrm{T}} \rangle$ e a multiplicidade de partículas carregadas N_{ch}. Ademais, o quadrado da velocidade do som c_s^2, uma quantidade termodinâmica de grande interesse que indica como um sistema responde a variações na densidade de energia, pode ser calculado em termos desses observáveis.

Apesar das extensas evidências experimentais acumuladas nos últimos anos para a produção de QGP em sistemas de colisão como ouro–ouro (AuAu) e chumbo–chumbo (PbPb), a formação desse meio em colisões de sistemas menores, como próton–chumbo (pPb), permanece uma questão em aberto. Nos últimos anos, observações experimentais em colisões pPb revelaram assinaturas semelhantes de dinâmica coletiva, levantando a questão sobre o surgimento do QGP em sistemas pequenos.

Este trabalho apresenta um estudo da correlação entre o momento transversal médio das partículas carregadas $\langle p_{\mathrm{T}} \rangle$ e a multiplicidade de partículas carregadas N_{ch} em colisões pPb a energias no centro de massa por par de núcleons de 5.02 TeV e 8.16 TeV, detectadas pelo experimento CMS no LHC. A análise dessa correlação em duas energias de colisão distintas permite a estimativa de c_s^2 em sistemas pPb, desde que se defina uma temperatura efetiva T_{eff} para o sistema com base no momento transversal médio. Dessa forma, o quadrado da velocidade do som é calculado para o sistema criado em colisões pPb como função da temperatura efetiva. Os resultados para $c_s^2(T_{\mathrm{eff}})$ são comparados com modelos não coletivos e hidrodinâmicos, com o objetivo de investigar o possível surgimento de um comportamento semelhante ao de um meio em sistemas pPb.

Os resultados obtidos para c_s^2 mostram-se aproximadamente compatíveis com cálculos de QCD na rede (lattice QCD), apresentando um aumento consistente do valor extraído de c_s^2 com T_{eff}, embora sejam sistematicamente superiores aos valores previstos pelo modelo hidrodinâmico. Em contraste, comparações com modelos que não incorporam efeitos de meio em colisões pPb apresentam um acordo muito pobre com os dados. Cortes cinemáticos no momento transversal p_{T} e na pseudorapidez η também são aplicados com o objetivo de estudar a robustez da metodologia e investigar diferentes regiões da produção de partículas.

Palavras-chaves: Colisões de Íons-Pesados. Análise de Dados. Quark-Gluon Plasma.

Abstract

Ultrarelativistic heavy-ion collisions create a substantial volume of a short-lived deconfined state of matter known as quark-gluon plasma (QGP). Furthermore, experiments carried by the Relativistic Heavy Ion Collider (RHIC) and Large Hadron Collider (LHC) have shown that the QGP produced in high-energy heavy-ion collisions behaves like a strongly coupled almost perfect fluid. Collective behaviour in collision systems can be studied by analyzing the correlation between the mean transverse momentum $\langle p_{\mathrm{T}} \rangle$ and charged-particle multiplicity N_{ch}. The speed of sound squared c_s^2, an interesting thermodynamic quantity which indicates how a system responds to variations in energy density, can be calculated in terms of these direct observables.

Despite the extensive experimental evidence gathered over the last years for the production of QGP in colliding systems such as gold-gold (AuAu) and lead-lead (PbPb), the formation of such a medium in the collision of smaller systems such as proton-lead (pPb) remains an open question. In recent years, experimental observations in pPb collisions have revealed similar signatures of collective dynamics, ultimately raising the question about the emergence of QGP matter in so called small systems.

This work presents a study of the correlation between the mean transverse momentum of charged particles $\langle p_{\mathrm{T}} \rangle$ and the charged-particle multiplicity N_{ch} in pPb collisions at center-of-mass energies of 5.02 TeV and 8.16 TeV, detected by the CMS experiment at the LHC. The analysis of this correlation at two different collision energies allows for the calculation of c_s^2 in pPb systems if one defines an effective temperature T_{eff} based on the mean transverse momentum. Thus, the speed-of-sound squared is calculated for the system created in pPb collisions as a function of this effective temperature. The results for $c_s^2(T_{\mathrm{eff}})$ are compared with non-collective and hydrodynamic models, in order to study the possible emergence of medium-like behaviour in pPb systems.

The results for c_s^2 are found to be approximately compatible with lattice QCD calculations, showing consistent increase of the extracted c_s^2 with T_{eff}, but are consistently higher than those predicted by the hydrodynamic model. However, comparisons with models that do not incorporate medium effects in pPb collisions show a very poor agreement with data. Kinematic cuts in transverse momentum p_{T} and pseudorapidity η are also applied as to study the robustness of the methodology and to study different regions of particle production.

Keywords: Heavy-Ion Collisions. Data Analysis. Quark–Gluon Plasma.

Nota de Imprensa

O estudo da matéria sob condições extremas de temperatura e densidade constitui um dos objetivos centrais da física nuclear e de partículas moderna. Em condições normais, quarks e glúons encontram-se confinados dentro de prótons e nêutrons, formando os constituintes fundamentais da matéria. No entanto, estudos teóricos e observações experimentais indicam que, quando a matéria nuclear é aquecida a temperaturas extremas, esses constituintes podem se desconfinar, dando origem a um novo estado da matéria chamado plasma de quarks e glúons (QGP).

As colisões de íons pesados a altas energias recriam o estado QGP da matéria, que conjectura-se ter preenchido o universo na escala de microssegundos após o Big Bang. Essa conexão com os primeiros momentos do universo, juntamente com a constatação de que a matéria primordial encontrada nessas temperaturas tinha que ser alguma nova forma de matéria não composta de hádrons, fornece fortes motivações para o estudo de colisões de íons pesados ultra-relativísticos.

A matéria QGP é criada em colisões entre núcleos pesados como colisões chumbo-chumbo (PbPb) no LHC. Além disso, resultados experimentais recentes sugerem que sistemas ainda menores, como quando um próton colide com um núcleo pesado, apresentam propriedades semelhantes aos sistemas de colisões de núcleos pesados. Essa semalhança em certos observáveis físicos levanta a questão: Um pequeno volume de QGP é formado em sistemas pequenos, como colisões próton-chumbo? Este projeto de mestrado buscou analisar dados de colisões pPb coletados pelo experimento CMS no CERN-LHC a fim de ajudar a esclarecer essa questão.

Analisamos dados de colisões próton-chumbo (pPb) em energias de centro-de-massa por par de nucleons de 5,02 TeV e 8,16 TeV, a fim de estudar a correlação entre o momento transversal médio $\langle p_{\mathrm{T}} \rangle$ das partículas de estado-final e do número de partículas carregadas criadas em cada colisão N_{ch}, e também estimar o valor aproximado da velocidade do som ao quadrado c_s^2, que contém informação sobre a equação de estado do sistema pós-colisão.

Um aspecto fundamental do trabalho é o método que utilizamos para determinar c_s^2, que emprega duas energias de colisão diferentes e a determinação das centralidades das colisões pPb com base na deposição de energia dos remanescentes da colisão nos detectores. Os resultados para c_s^2 como função da temperatura efetiva do sistema T_{eff} são indicados na

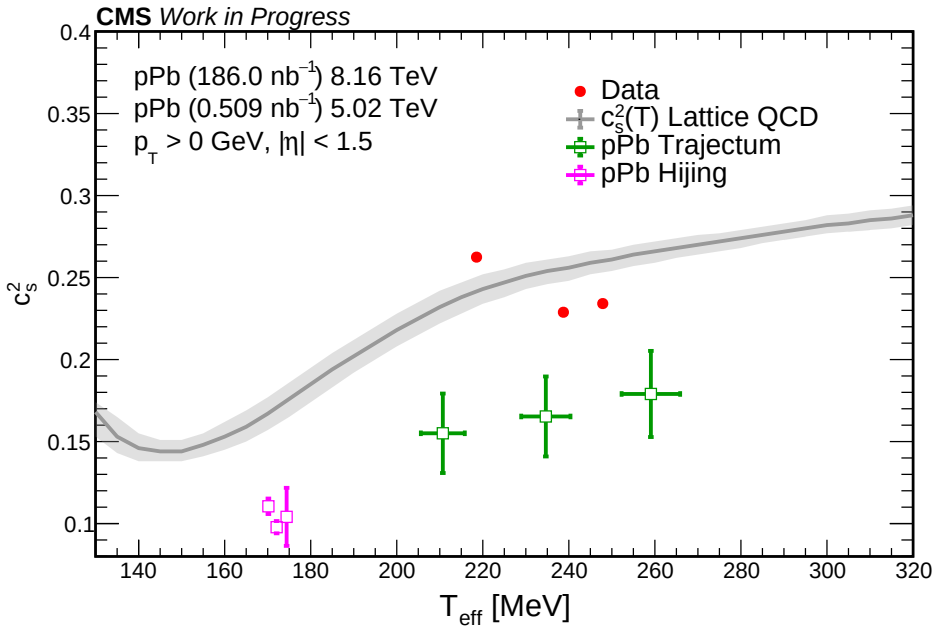


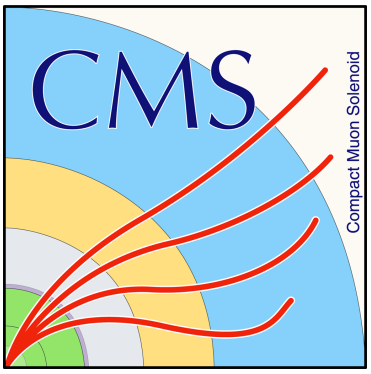
Figura abaixo, que considera apenas incertezas estatísticas. Os valores de c_s^2 obtidos para cada centralidade são comparados com dois modelos físicos diferentes: O modelo HIJING, que não incorpora a descrição hidrodinâmica da formação de um fluido na colisão, e o modelo TRAJECTUM que descreve a evolução de um fluido criado na colisão.

Este trabalho visa contribuir para o estudo das propriedades do QGP em sistemas de colisões de pequena escala como pPb e outros, a fim de ajudar a refinar modelos teóricos de colisões nucleares de alta energia e a aprimorar nossa compreensão das propriedades fundamentais da matéria governadas pela força nuclear forte.

Esta pesquisa foi realizada no âmbito da Colaboração CMS, um dos experimentos principais do CERN-LHC, e foi financiada pelo Conselho Nacional de Desenvolvimento Científico e Tecnológico (CNPq).

E-mail para contato: lucasdoriadecarvalho@gmail.com.

This work analyzes unpublished data collected by the CMS experiment. Moreover, it wasn't subject for approval through internal CMS collaboration proceedings. All plots are therefore properly labeled with "**CMS** *Work in Progress*".



Sumário

1 Introduction 11

2 Theory of heavy-ion collisions and QGP formation 13

2.1 The QCD phase-diagram 13

2.2 The standard model of heavy-ion collisions 16

2.3 Thermodynamics of the QGP in heavy-ion collisions 19

2.4 Collectivity in pPb systems 22

3 The CMS experiment at the CERN-LHC 23

3.1 The Large Hadron Collider 23

3.2 The CMS experiment 26

3.3 The CMS coordinate system and collision observables 29

3.4 Trigger system for data acquisition 31

4 Measurement methodology and data analysis framework . . . 33

4.1 Online and offline event selections 33

4.2 Control plots 36

4.3 Centrality estimation 41

4.4 Fit and extrapolation of p_T spectrum 44

4.5 Assessing the correlation between $\langle p_T \rangle$ and N_{ch} 46

4.6 Systematic uncertainties 51

5 Results and insights 52

6 Conclusion 56

Bibliography 57

APPENDIX A – Numerical results 65

1 Introduction

Quantum chromodynamics (QCD), the theory of the strong interaction, predicts a phase-transition at a critical temperature $T_c \sim 155$ MeV [1] from hadronic matter to a deconfined state of quarks and gluons, called the quark-gluon plasma (QGP) [2]. It is conjectured that this QGP matter existed in the very early stages of universe evolution [3], and that QGP matter could also be found in the inner core of massive neutron starts [4].

The conditions for the phase-transition from hadronic matter to QGP are reached in high-energy heavy-ion collisions, where the extreme amount of energy density deposited in the system allows for the production of QGP [5], making relativistic and ultrarelativistic heavy-ion collisions a unique environment to study the properties of strongly interacting matter.

Remarkably, it has been reported that the QGP created in ultrarelativistic lead-lead (PbPb) collisions behaves like a strongly coupled fluid that can be described by relativistic hydrodynamics [6]. Two of the main observables in heavy-ion collisions that reflect the collective behaviour of this medium are the mean transverse momentum of final state charged particles $\langle p_{\mathrm{T}} \rangle$ and the charged particle multiplicity N_{ch} which can be related to the thermodynamic properties of the QGP.

One of the fundamental quantities governing the macroscopic behavior of such a medium is the speed-of-sound squared c_s^2, defined as $dP/d\epsilon$, which encodes the response of the pressure P to changes in energy density ε. The speed of sound directly reflects the equation of state (EoS) of QGP matter formed in high-energy heavy-ion collisions and is therefore sensitive to the underlying degrees of freedom and to the thermodynamic properties of the medium. In particular, lattice QCD calculations predict a characteristic temperature dependence of c_s^2, with a suppression near the crossover region and a gradual increase toward the ideal gas limit $c_s^2 = 1/3$ at higher temperatures.

It has been proposed that the speed of sound in the QGP can be approximately estimated using experimental observables available at particle detectors such as the charged-particle multiplicity N_{ch} and the average transverse momentum $\langle p_{\mathrm{T}} \rangle$ of emitted charged particles [7, 8]

$$c_s^2 = \frac{dP}{d\epsilon} = \frac{s\,dT}{T\,ds} = \frac{d\ln\langle p_{\mathrm{T}}\rangle}{d\ln N_{\mathrm{ch}}}. \tag{1}$$

While the existence of the QGP is well established in large collision systems such as PbPb, recent experimental observations have revealed signatures of collective behavior in much smaller systems, including proton-lead (pPb) and even proton-proton (pp) collisions at high charged-particle multiplicity [9–11].

In this context, the extraction of medium-sensitive quantities such as the speed-of-sound in small collision systems provides a powerful and complementary probe. The speed of sound is directly related to the equation of state and can be accessed through correlations between global event properties. In particular, the relationship between the mean transverse momentum $\langle p_T \rangle$ and the charged-particle multiplicity N_{ch} offers a way to study the thermodynamic response of the system to changes in entropy.

This work presents a measurement of the speed-of-sound squared c_s^2 in pPb collisions at center-of-mass energies of 5.02 TeV and 8.16 TeV, using data collected by the CMS experiment during LHC Run 2. The analysis is based on the correlation of $\langle p_{\mathrm{T}} \rangle$ and N_{ch}. Moreover, an effective temperature T_{eff} is defined for the system after the collision and the quantity $d\ln\langle p_{\mathrm{T}} \rangle / d\ln N_{\mathrm{ch}}$ is extracted. This observable is then interpreted, within well-defined assumptions, and compared to non-collective models as well as hydrodynamic models, providing further insight into the properties of the system.

The structure of this dissertation is as follows. Chapter 2 discusses the theoretical background relevant to the experimental analysis described in the rest of the work, with particular emphasis on probing the thermodynamic properties of the collision system using bulk observables such as $\langle p_{\mathrm{T}} \rangle$ and N_{ch}. Chapter 3 gives an introduction to the CMS detector at the CERN-LHC, which was the experiment in which the collision data was collected. Chapter 4 describes the set of triggers (online selection) used by the experiment in data acquisition and offline event selection along with the methodology applied in the measurement of c_s^2. In particular, the p_{T} distributions for the reconstructed tracks are classified into centrality bins for a more robust analysis. The energy deposited in the hadron-forward calorimeters is used as event-activity proxies, and the relation between experimental observables and thermodynamic properties of the system is explored. Finally, the results and their interpretation are discussed in Chapter 5, followed by the conclusions of the work.

2 Theory of heavy-ion collisions and QGP formation

In this Chapter, the main ideas of quantum chromodynamics (QCD) that are relevant to the work are discussed, such as the QCD phase-diagram and the phase-transition to the quark-gluon plasma (QGP). The standard model of heavy-ion collisions is also introduced, as it serves as a theoretical background for understanding the different stages of the system after the collision and the general picture. The hydrodynamic phase of the system is explained in the context of the QGP observed in PbPb systems, and the possibility of a similar medium in pPb systems is discussed, pointing to the collective behaviour observed so far. The concepts necessary to interpret the experimental measurements and subsequent analysis of collision data are also explained, focusing on the direct experimental observables measured by particle detectors in heavy-ion collisions, such as the particle multiplicity and transverse momentum of emitted particles.

2.1 The QCD phase-diagram

The strong interaction is one of the four fundamental forces of nature and is responsible for binding quarks and gluons into hadrons, as well as for holding nucleons together inside atomic nuclei. The theory that describes the strong force is called quantum chromodynamics (QCD), a non-abelian gauge-theory based on the symmetry group $SU(3)$. [12] In QCD, the strong force acts on particles that carry color charge, namely quarks and gluons, through the exchange of spin-1 massless gluons.

The need for a fundamental theory of the strong interaction emerged in the 1950s, when a large number of strongly interacting particles were discovered. [13] In 1961, Gell-Mann introduced the Eightfold Way, a way of arranging the plethora of hadrons into geometrical patterns based on their charge and strangeness. [14] Based on this idea, Gell-Mann and Zweig independently proposed that all hadrons are in fact composed of even more elementary constituents, the quarks. [15] The quark model asserts that every baryon is composed of three quarks, and every meson is composed of a pair quark-antiquark $q\bar{q}$. In 1972, Gell-Mann, Fritzsch and Leutwyler developed a gauge-theory in which the interaction of quarks is mediated by the exchange of massless bosons[1], later labeled gluons, which also

[1] Bosons are particles with integer spin values, such as $s = 0, 1$. Bosons are force-carrying particles that follow the Bose-Einstein statistics such as gluons, photons and the Z and W bosons. Fermions, on the

carry color charge. Moreover, it was shown by Hooft and Veltman that non-abelian gauge theories are renormalizable [16], which means the QCD can be made free of infinities by a finite number of redefinitions of the parameters and fields, ultimately solidifying the theory.

The theory of QCD is characterized by a coupling strength α_s which is not constant, but instead depends on the energy scale of the interaction. One of the most interesting aspects of QCD is that of asymptotic freedom, discovered in 1973 by Gross, Wilczek, and Politzer [17, 18]. The observed phenomenon of asymptotic freedom of QCD implies that interactions between quarks and gluons become weaker as the energy scale increases and the distance scale decreases. This is due to the fact that the coupling strength α_s weakens for interactions between quarks and gluons at very high energies. At low energies, color confinement takes place and QCD matter (quarks and gluons) is confined into colorless hadrons, which prevents quarks and gluons from being observed as free particles. However, due to asymptotic freedom, QCD predicts a phase-transition from hadronic matter to a deconfined state known as the quark-gluon plasma (QGP).

The phase-diagram for QCD matter is shown on Figure 1 as a function of temperature T and baryon chemical potential μ_{B}. Lattice QCD calculations[2] predict a crossover transition from hadronic matter to QGP at $T_{\mathrm{c}} \sim 155$ MeV and zero μ_{B}, in which conditions the energy density exceeds the threshold for deconfinement. These conditions can be achieved in high-energy nuclear collisions at the LHC. Other experiments at lower energies also allow us to map the phase-diagram at higher μ_{B} regions, and one of their main objectives is the study of a possible first-order phase transition at higher baryon doping. [19]

Because this change is not merely microscopic but collective, it manifests itself in the macroscopic thermodynamic properties of the system. Quantities such as pressure, energy density, entropy density, and their derivatives encode the underlying structure of the medium and provide essential information about the phase transition, making them key observables for identifying the formation of deconfined QCD matter in high-energy collisions. Figure 2 shows lattice QCD calculations for energy density ϵ, pressure p and entropy density s for strongly interacting matter, showing the continuous phase-transition

other hand, are particles with half-integer spin values, such as $s = \frac{1}{2}, \frac{3}{2}$ and are matter particles like the quarks and leptons, which follow the Fermi-Dirac statistics.

[2] Lattice QCD is a non-perturbative formulation of QCD that discretizes spacetime into a lattice, allowing first-principles numerical calculations of strongly interacting matter.

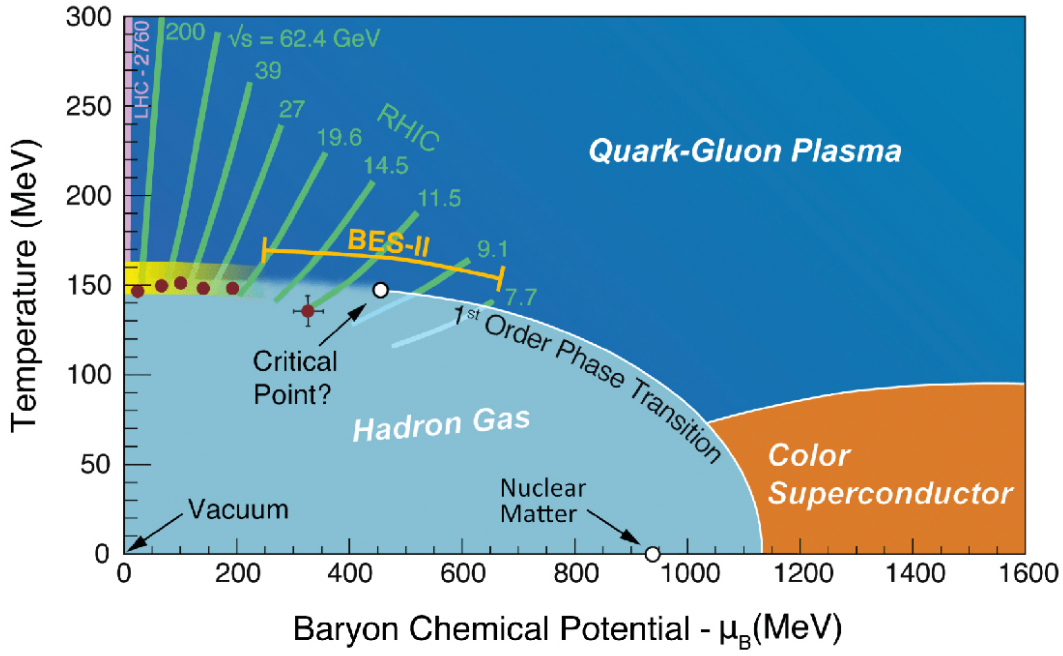


Figure 1 – The phase-diagram of QCD as a function of temperature T and baryon doping, the excess of quarks over antiquarks, parametrized by the chemical potential for baryon number μ_{B}. Adapted from [3].

above T_{c} from a hadron resonance gas (HRG) at lower temperatures to a state of QGP matter at high temperatures and how thermodynamic properties can be used to probe this transition.

Because QCD is asymptotically free, thermodynamic quantities approach the Stefan-Boltzmann limit at sufficiently high temperatures, corresponding to a system of weakly interacting quarks and gluons. In this non-interacting limit bulk observables such as the energy density and entropy density attain their ideal-gas values. However, in the temperature range relevant for heavy-ion collisions, lattice QCD calculations show that these quantities remain approximately 20% below their Stefan-Boltzmann limits, indicating that the QGP behaves as a strongly coupled medium rather than a weakly interacting gas. The rapid increase observed in ε/T^4 and s/T^3 from Figure 2 reflects the crossover transition from a hadron resonance gas to a deconfined QGP, where the liberation of color degrees of freedom leads to a significant enhancement in the effective number of thermodynamic degrees of freedom. Experimentally constraining ε/T^4 remains a major challenge. While hydrodynamic modeling constrained by hadronic observables provides information on the time evolution of the energy density, current measurements do not yet

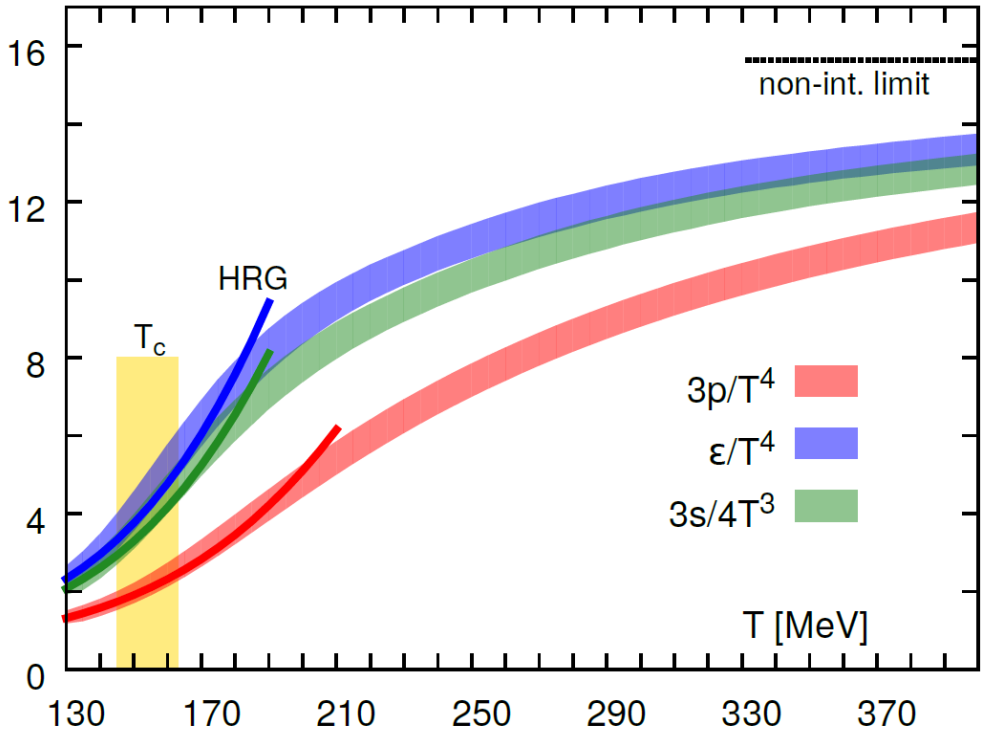


Figure 2 – Lattice QCD calculations for energy density ϵ, pressure p and entropy density s for strongly interacting matter. Values for a hadronic resonance gas (HRG) are shown as continuous lines and for QGP matter as bands. The rapid increase observed in ε/T^4 and s/T^3 from Figure 2 reflects the crossover transition from a hadron resonance gas to a deconfined QGP. Due to asymptotic freedom, thermodynamic quantities approach the Stefan-Boltzmann limit at sufficiently high temperatures [3].

determine T with sufficient precision to directly resolve the expected rise in the number of degrees of freedom across the transition.

2.2 The standard model of heavy-ion collisions

The physics of heavy-ion collisions and the evolution of the system are described by the standard model of heavy-ion collisions. [20] This section briefly describes the most important aspects of the model relevant to this work.

In a particle accelerator such as the Large Hadron Collider (LHC), the particles are accelerated to relativistic and ultrarelativistic energies along the beam axis. The four-momentum of a particle in the beam is given by

$$p^\mu = (E, \vec{p}), \qquad E = \sqrt{p_x^2 + p_y^2 + p_z^2 + m^2} = \sqrt{p_\mathrm{T}^2 + p_z^2 + m^2}, \tag{2}$$

where E is the total energy of the particle and p_{T} is the component of the momentum orthogonal to the beam axis. Generally, the beam axis corresponds to the z axis of a cylindrical coordinate system. This leads to the definition of quantities that have the desirable property of boost invariance along the z axis. This is the case of rapidity, which is defined by

$$y = \frac{1}{2} \ln \left(\frac{E + p_z}{E - p_z} \right). \tag{3}$$

The rapidity is zero for particles with $p_z = 0$, which means their momentum has components only along the transverse plane relative to the beam axis, but tends to $\pm\infty$ when a particle is moving close to the beam axis in either direction. For ultrarelativistic collisions, i. e. the energy of the particles are much greater than their rest mass $E \gg m$ and Equation 2 reduces to $E \approx p$.

Another important quantity is the pseudorapidity η of a particle, defined by

$$\eta = -\ln \tan \left(\frac{\theta}{2} \right), \qquad \cos(\theta) = \frac{p_z}{p}, \tag{4}$$

For ultrarelativistic collisions $\eta = y$. Furthermore, the pseudorapidity is preferred experimentally since it depends only on the particle's polar angle between the beam axis and the transverse plane, as shown in the right-side of Eq. 4.

The energy available for the production of particles in an ultrarelativistic collision, where two beams of circulating particles are made to interact at some collision point, is given by the center-of-mass (CM) energy measured in the laboratory frame. If the beams have different energies per nucleon E_1 and E_2, the total CM energy is given by

$$E = 2\sqrt{E_1 E_2} \tag{5}$$

The CM energy per nucleon pair is more commonly denoted by $\sqrt{s_{\mathrm{NN}}}$. Proton-proton and heavy-ion collision are generally considered ultrarelativistic for $\sqrt{s_{\mathrm{NN}}} > 10$ GeV. The first experiments with ultrarelativistic heavy-ions took place at the Brookhaven National Laboratory (BNL) and at the European Organization for Nuclear Research (CERN) in 1986. The Alternating Gradient Synchrotron (AGS) at BNL accelerated beams of Si^{28} at 14 GeV per nucleon. At CERN, the Super Proton Synchrotron (SPS) accelerated O^{16} at 60 and 200 GeV per nucleon pair in 1986 [21, 22]. Currently the Large Hadron Collider (LHC) at CERN provides the highest collision energies available with Pb beams

accelerated up to 5.36 TeV, enabling precision studies of the quark–gluon plasma (QGP) at extreme temperatures and energy densities. Lower-energy facilities also play a crucial and complementary role, with the RHIC currently exploring the temperature–baryon density dependence of QCD matter, notably through its Beam Energy Scan (BES) program, which targets the onset of deconfinement and the possible location of a critical point in the QCD phase diagram [19]. At even lower energies, the SPS at CERN contributes with key measurements on strangeness production and collective phenomena [23].

At the moment of collision, each nucleus can be visualized as a Lorentz contracted disc. For large nuclei such as Pb or Au, the diameter of the disc is about 14 fm [3] and its thickness is about $14/\gamma$ fm. Moreover, at high-energy scales, the nucleons can't be described only by the valence u and d quarks because the area density of quarks, antiquarks and gluons (partons for short in the language of Feynman) increases with the velocity of the nuclei, and thus the incident nuclei are highly complex systems of partons with a longitudinal momentum distribution[3]. When the two Lorentz contracted discs overlap or collide, most of the incident partons lose some energy but are not kicked by any large angle. These interactions are called soft-interactions, meaning that they involve little transverse momentum transfer. [20]

The current picture of the standard model of heavy-ion collisions is that after the collision the system reaches local thermodynamic equilibrium after a time τ_0 [24–27], which is the proper time it takes for the system to be thermalized. After thermalization, one can properly define thermodynamic quantities such as temperature T, pressure P and entropy density s for the system. The average energy density ϵ in this expanding system after the collision, at time τ_0 can be estimated using the Bjorken formula [5],

$$\epsilon = \frac{dE_{\mathrm{T}}}{dy}\,\frac{1}{\tau_0 A_\perp} \tag{6}$$

where $A_\perp$ is the transverse overlap area of the two nuclei and dE_{T}/dy is the transverse energy per unit rapidity. For lead-lead (PbPb) systems, the reference value for the thermalization time τ_0 is ~ 1 fm. For the 5% most central PbPb collisions at $\sqrt{s_{\mathrm{NN}}} = 2.76$ TeV, the Bjorken formula gives energy densities up to 14 GeV/fm^3 [28]. This value is well above the expected threshold of $\epsilon_{\mathrm{QGP}} > 1$ GeV/fm^3 for the production of a quark-gluon plasma estimated from lattice QCD calculations [29].

[3] In high-energy physics, the longitudinal momentum distribution of quarks and gluons inside hadrons has to be described by the parton distribution functions (PDFs).

One of the most interesting results about the QGP produced in ultrarelativistic heavy-ion collisions is the observation of collective phenomena. Because the estimated energy density and temperature reached in the collisions, it was already expected that matter would not be made of hadrons and instead to show color degrees of freedom, because of asymptotic freedom. However, at the temperatures that have been achieved in heavy-ion collisions to date, the matter is not a weakly coupled QGP as originally expected. Instead, the system formed in ultrarelativistic heavy-ion collisions behaves like a medium made up by a strongly coupled relativistic fluid that exhibits collective flow phenomena [30].

Some key signatures supporting the formation of this strongly coupled QGP in central[4] PbPb collisions include the observation of strong azimuthal anisotropies in particle emission [31] and the scaling behavior of bulk observables, such as the transverse momentum of emitted particles p_{T}, with collision centrality [32–34]. These measurements are consistently described by relativistic hydrodynamic models, suggesting that the produced medium reaches approximate local equilibrium and evolves collectively [6].

Each elemental volume of QGP expands hydrodynamically while decreasing the energy density and temperature of the medium until it reaches the hadronic freeze-out at around $\tau_{\mathrm{f.o.}} \sim 10$ fm [35], in which QCD confinement transition occurs and quarks and gluons are hadronized and the hadrons ultimately move toward the detectors of the experiment. Figure 3 illustrates the picture of the standard model of heavy-ion collisions with the different stages after an ultrarelativistic collision.

2.3 Thermodynamics of the QGP in heavy-ion collisions

As stated in Section 2.2, the QGP formed in ultrarelativistic lead-lead (PbPb) collisions has characteristics of a strongly coupled fluid that are reflected in final state observables, indicating collective behaviour of the medium. The collective dynamics and macroscopic properties of this QGP are well described by the principles of nearly ideal relativistic hydrodynamics. Since the system is approximately thermalized, the system can be described by the equation of state (EoS), which relates the energy density ϵ and the pressure P. The EoS essentially gives information about how the medium responds to

[4] As it will be discussed later, the centrality refers to the degree of overlap of the incident nuclei, and it defines the initial energy density and effective volume of the produced medium.

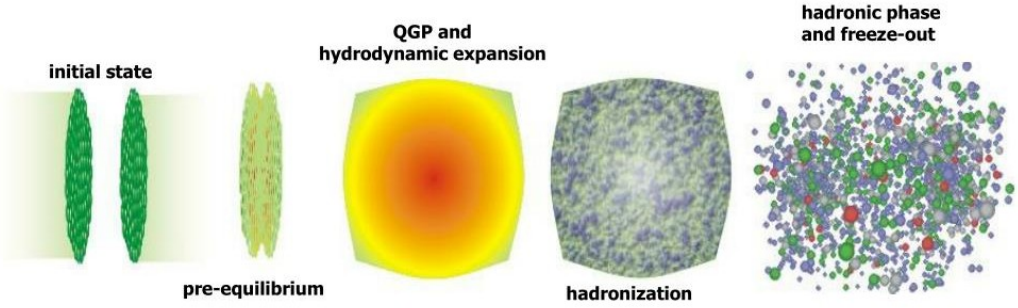


Figure 3 – Different stages of ultrarelativistic heavy-ion collisions. Shortly after the collision, the system goes under a quick phase of thermalization, and is described by relativistic hydrodynamics. After the freeze-out, the hadrons move radially outward to the detectors. Adapted from [36].

changes in its energy density. One of the ways to study the EoS of a relativistic fluid is by determining the squared speed of sound c_s^2 in the medium, which is defined by

$$c_s^2 = \left(\frac{\partial P}{\partial \epsilon}\right) \tag{7}$$

For a baryonless fluid such as the QGP, the change in pressure is just $dP = sdT$ and the change in energy density is just $d\epsilon = Tds$ [26]. Thus, one can calculate the squared speed of sound in the QGP as

$$c_s^2 = \frac{s\,dT}{T ds} = \frac{dT}{T}\,\frac{s}{ds} = \frac{d\ln T}{d\ln s} \tag{8}$$

However, the determination of both the temperature T and entropy density s in the system created in heavy-ion collisions is a very difficult task [37]. As it will be discussed in Chapter 3, one only measures the final-state particles that reach the detectors, after the hadronization, and thus the temperature and energy density of the QGP are not direct experimental observables. This means the QGP needs to be studied in terms of experimental observables that in turn can serve as proxy for the thermodynamic properties of the medium.

If one considers the limiting picture of a non-interacting QGP (which corresponds to the massless ideal-gas limit) the total energy per particle, in a system that follows Boltzmann statistics, is $u = 3\,T$ [38]. Considering the ultrarelativistic limit for particles produced near mid-rapidity ($\eta \sim 0$), we have by Eq. 2 that $E \approx p_{\mathrm{T}}$. Therefore, a

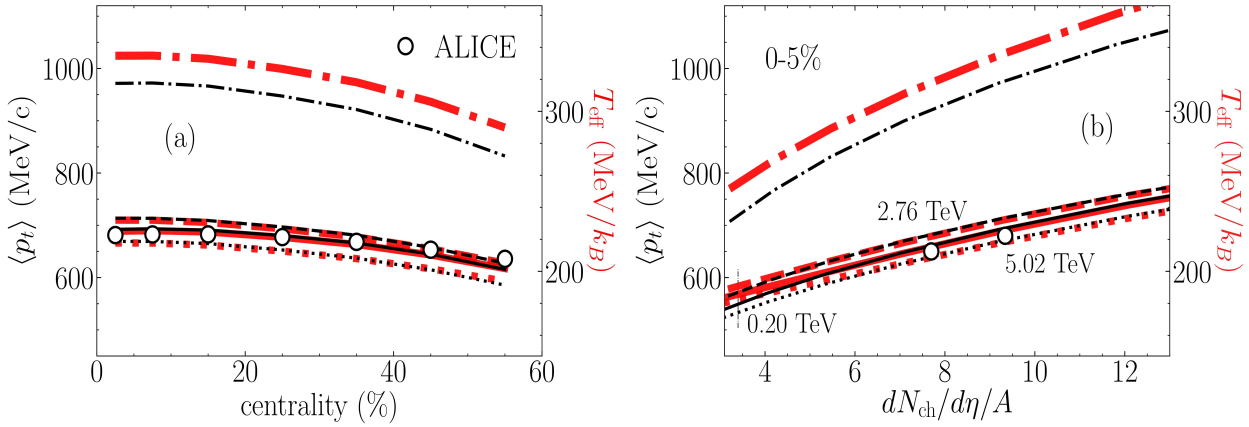


Figure 4 – Results of hydrodynamic simulations of the correlation between the charged-particle mean transverse momentum $\langle p_{\rm T} \rangle$ and effective temperature $T_{\rm eff}$ of the QGP formed in PbPb collisions. Black curves correspond to $\langle p_{\rm T} \rangle$ and red curves to the effective temperature $T_{\rm eff}$. (a) Results are presented as a function of the collision centrality for a fixed energy per nucleon–nucleon collision of $\sqrt{s_{\rm NN}} = 5.02$ TeV. (b) Results are presented as a function of the collision energy for a fixed centrality range (5% most central collisions). The variable on the horizontal axis is the multiplicity of charged particles in the pseudorapidity interval $|\eta| < 1.5$. Adapted from [7].

reasonable approximation to the effective temperature of the QGP in ultrarelativistic heavy-ion collisions at mid-rapidity is

$$T_{\rm eff} \approx 0.33 \, \langle p_{\rm T} \rangle \tag{9}$$

To verify this expectation, hydrodynamic simulations of PbPb collisions were carried out by Gardim et. al [7] using different equations of state for the QGP. The results of the simulations are adapted in Figure 4, confirming the expectation that the effective temperature $T_{\rm eff}$ is tightly correlated with the mean transverse momentum of charged particles $\langle p_{\rm T} \rangle$. The most important result is that the simulations indicate a direct proportion of $\langle p_{\rm T} \rangle = 3.07 \, T_{\rm eff}$, which holds irrespective of transport coefficients. This proportionality is satisfied for all collision centralities and for most of the considered range of collision energies. Combining their simulation results with the experimental result $\langle p_{\rm T} \rangle = 681$ MeV the authors are able to estimate the effective temperature of the QGP in central PbPb collisions at $\sqrt{s_{\rm NN}} = 5.02$ TeV to be $T_{\rm eff} \approx 222 \pm 9$ MeV.

Another direct observable accessible to a collision experiment is the charged-particle multiplicity $N_{\rm ch}$, which is proportional to the total number of particles produced in the collision [39, 40]. The charged-particle multiplicity can also serve as a probe to the entropy density s in the QGP via the relation [7]

$$\frac{ds(T_{\text{eff}})}{s} = \frac{dN_{\text{ch}}}{N_{\text{ch}}} \tag{10}$$

2.4 Collectivity in pPb systems

Small collision systems such as proton–proton (pp) and proton–nucleus (pA) were expected to be too short-lived and insufficiently dense to produce a thermalized QGP. However, measurements at the LHC have revealed a range of collective phenomena in high-multiplicity pp and pPb collisions that closely resemble effects previously associated with QGP formation in heavy-ion collisions.

The formation of a collective medium in pPb collisions can be visualized in momentum anisotropies of particles produced in heavy ion collisions. If the quarks and gluons form a strongly coupled liquid which thermalizes after some time, the distribution of energy density produced in the collision remains anisotropic, and this causes a pressure-driven expansion that is reflected in the distribution of p_{T}, leading to momentum anisotropies in the system.

This effect can be quantified using a Fourier decomposition of the azimuthal particle distribution, where the so-called flow coefficients v_n characterize the magnitude of the anisotropic flow. In hydrodynamic descriptions, the presence of non-zero v_n coefficients is a direct consequence of pressure-driven collective expansion and reflects collective behaviour in the system.

The observation of significant anisotropic flow coefficients in high-multiplicity pPb collisions [10, 11], comparable in magnitude to those measured in peripheral PbPb collisions at similar charged-particle multiplicities, therefore suggests that pressure gradients are present in the dynamical evolution of these small systems. This behavior is difficult to reconcile with models based solely on independent particle production and instead points to the presence of strong final-state interactions capable of sustaining collective motion. Measuring the speed of sound squared in such a system can thus offer insight into the effective thermodynamic properties of matter formed in pPb collisions [41].

3 The CMS experiment at the CERN-LHC

The proton-lead (pPb) collision data analyzed in this work was collected by the CMS experiment at the LHC. In this chapter, the CMS detector is presented. The detector's overall design and structure are shown, emphasizing the tracking system and hadron-forward (HF) calorimeters, which are described in detail, since they compose the most important systems for the analysis. The tracking reconstruction and trigger system is also highlighted, in order to better discuss the set of triggers and event-selection described in Chapter 4.

3.1 The Large Hadron Collider

The Large Hadron Collider (LHC) is currently the world's largest and most powerful particle accelerator, consisting of a 27 km ring of superconducting magnets with a number of accelerating structures to boost the energy of the particles along the way. The accelerator sits at around 100 m underground at the European Organization for Nuclear Research (CERN), on the Franco-Swiss border near Geneva, Switzerland. [42] The LHC is designed to accelerate protons to an energy up to 6.5 TeV by powerful electric fields generated in radio frequency cavities and guided around their circular orbits by superconducting dipole magnets with magnitude of 8.33 T in tubes under very high vacuum.

The CERN accelerator complex is depicted in Figure 5. The protons that are accelerated in the LHC initially come from the Linac4[1], where hydrogen atoms are ionized and accelerated to an energy of 50 MeV before being injected on the PS Booster (PSB). The PSB accelerates them to 1.4 GeV and the beam is then fed to the Proton Synchrotron (PS), where it is accelerated to 25 GeV. Protons are then sent to the Super Proton Synchrotron (SPS) where they are accelerated to 450 GeV. Finally, the protons are injected in the LHC tunnel from the SPS (both in a clockwise and anticlockwise direction) where they are accelerated to energies up to 6.5 TeV [43].

Since this analysis works with pPb collisions, it is interesting to also mention how the lead-ions are injected on the LHC tunnel. The Pb ions are produced from a highly purified lead sample heated to a temperature of about 800°C. This produces a lead vapour

[1] This work uses data from the Run 2 of the LHC, which still used the Linac2 as the hydrogen ion booster. However, the Linac2 was substituted by the Linac4 in 2018.

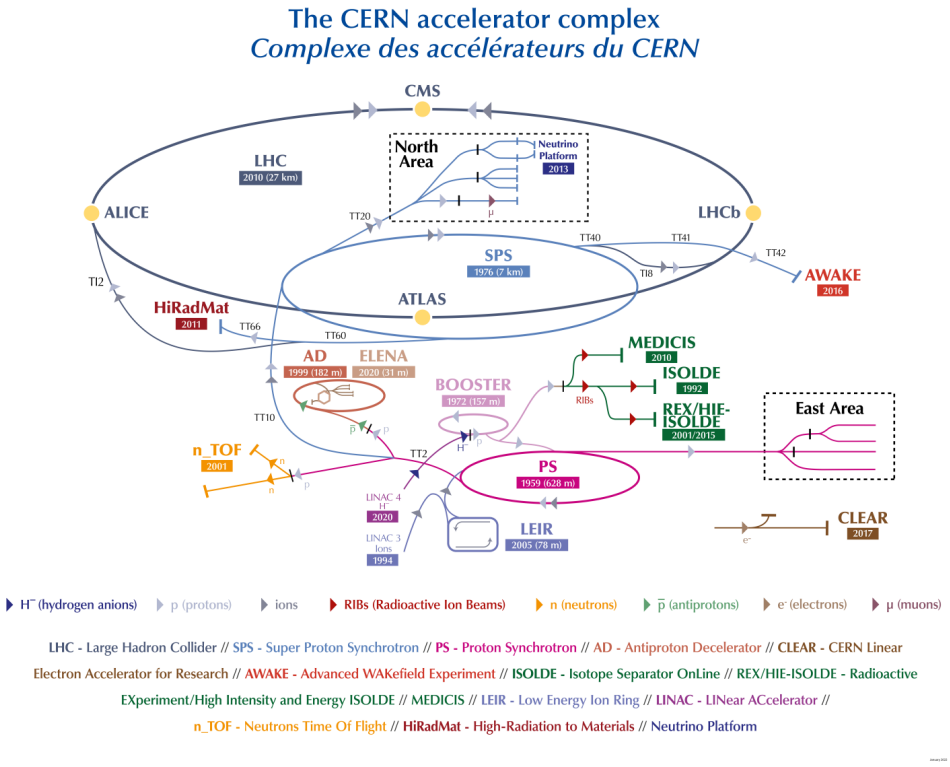


Figure 5 – The CERN accelerator complex. Each accelerator boosts the energy of a beam of particles before injecting the beam into the next machine in the sequence. In the Large Hadron Collider (LHC), particle beams are accelerated up to the energy of 7 TeV per nucleon. Most of the other smaller accelerators in the chain have their own experimental halls where beams are used for experiments at lower energies. From the CERN Document Server.

that is ionized, selected and accelerated to 4.2 MeV/u (energy per nucleon) before passing through a carbon foil, which strips most of them to Pb^{54+}. The Pb^{54+} beam is accumulated, then accelerated to 72 MeV/u in the Low Energy Ion Ring (LEIR), which transfers them to the PS. The PS accelerates the beam to 5.9 GeV/u and sends it to the SPS after first passing it through a second foil where it is fully stripped to Pb^{82+}. The SPS accelerates it to 177 GeV/u and then sends it to the LHC, which accelerates it to 2.56 TeV/u. [44]

The hadronic beams that are injected on the LHC tunnel via the SPS are structured in 2808 bunches in the case of a beam of protons, and 592 bunches for a beam of Pb^{82+}.[2] [45] Each bunch contains around 1.1×10^{11} protons or 7×10^{7} ions spaced by 25 ns. These bunches are made to cross through each other (bunch crossing) on different interaction points located along the LHC tunnel.

[2] The bunch structure of a modern accelerator is a direct consequence of the radio frequency (RF) acceleration scheme. The hadrons can only be accelerated when the RF field has the correct orientation when particles pass through an accelerating cavity, which happens at well specified moments during an RF cycle.

The number of collisions per second N_{event} for a given experiment is proportional to the cross-section for the observed event σ_{event}. The proportionality factor between the number of events per second and the cross-section is called the instantaneous luminosity L, [46]

$$N_{\text{event}} = L\,\sigma_{\text{event}} \tag{11}$$

The luminosity is thus a measure of how well the accelerator can produce the desired events of a given experiment. The nominal design peak luminosity for PbPb collisions at 2.56 TeV/u at the LHC is 10^{27} cm^{-2} s^{-1} and 2×10^{34} cm^{-2} s^{-1} for pp collisions at 14 TeV. The luminosity reflects the collision rate for a given process.

The number of total observed events $N_{\text{total events}}$ is related to the integrated luminosity of the experiment [47],

$$N_{\text{total events}} = \mathcal{L}\,\sigma_{\text{event}} \tag{12}$$

The integrated luminosity $\mathcal{L}$ is a measure of the total volume of data produced by the experiment. It is most commonly measured in units of inverse barns, where the conversion factor is 1 b^{-1} = 10^{24} cm^{-2}.

The LHC has four main experiments, which are the CMS, ATLAS, ALICE and LHCb, located in different interaction points along the LHC tunnel.[3] The beams inside the LHC are made to collide at these four interaction points around the accelerator ring, corresponding to the positions of the four particle detectors.

The LHC operation is structured in multi-year "Runs" separated by "Long Shutdowns" (LS) in order to balance data collection with the technical demands of maintaining and upgrading the accelerator. The Long Shutdowns allow for the infrastructure upgrade of the LHC in order to install more powerful magnets or sensitive detectors to reach higher energies (e.g., jumping from 8 TeV in Run 1 to 13 TeV in Run 2 for pp collisions). Each Run generates an immense amount of data that take years to fully analyze. Thus, structuring work into Runs create stable periods of data-taking followed by periods to analyze the results.

[3] The experimental collaborations are individual entities, funded independently from CERN. Each experiment is a member of CERN, which contributes to the maintenance and operation budget of the LHC experiments.

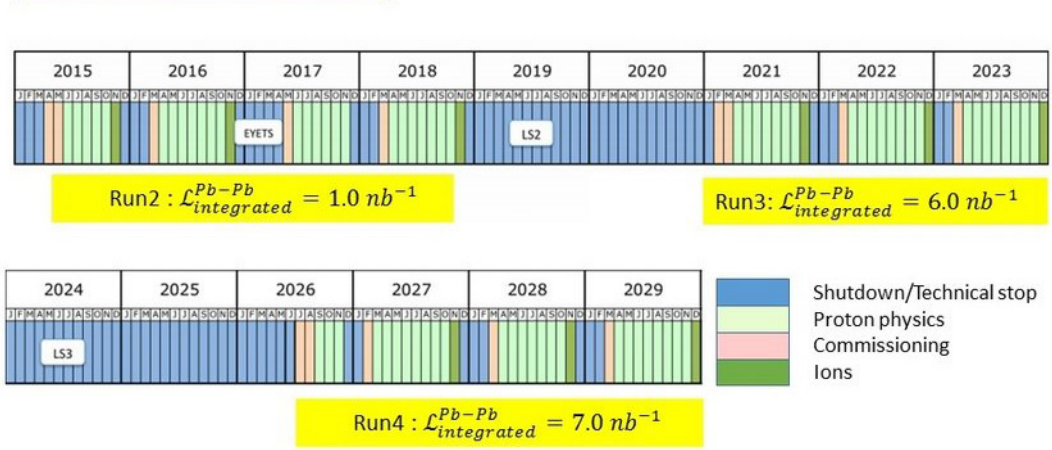


Figure 6 – Representation of different phases of the LHC schedule for the next years. The integrated luminosity of PbPb experiments for the Runs 2 and 3 are shown, along with the projected luminosity for the Run 4. Adapted from [48].

3.2 The CMS experiment

The Compact Muon Solenoid (CMS) is a general-purpose and nearly hermetic detector located at the interaction point number five (IP5) of the LHC tunnel at CERN. It has a length of 21.6 m, a diameter of 14.6 m, and a total weight of 12500 t. [49] The detector is built around a state-of-the-art superconducting solenoid that generates a strong magnetic field of 3.8 T. The CMS collaboration operates and collects data from the CMS detector, and it is one of the largest international scientific collaborations in history, involving about 5500 particle physicists, engineers, technicians, students and support staff from 241 institutes in 54 countries, including Brazil and UFRGS.

The CMS experiment is designed to investigate a wide range of physics, ranging from the Standard Model, which include the Higgs boson discovery achieved in 2012 simultaneously with the ATLAS experiment [50, 51], as well as search for new particles signs of BSM physics. Recently, the CMS collaboration was successful on the most precise measurement of the W boson mass at the LHC, based on a sample of proton-proton (pp) collisions at a center-of-mass energy of 13 TeV. [52] One of the main goals of the CMS experiment is to study the high-density QCD matter produced in heavy-ion collisions. [53] A recent measurement by the CMS experiment of the speed-of-sound squared c_s^2 in the system created in head-on PbPb collisions at $\sqrt{s_{\mathrm{NN}}} = 5.02$ TeV showed very well agreement with lattice QCD calculations, indicating the production of a deconfined phase of matter at extremely high temperatures. [54] Studies of possible QGP formation and similar collective

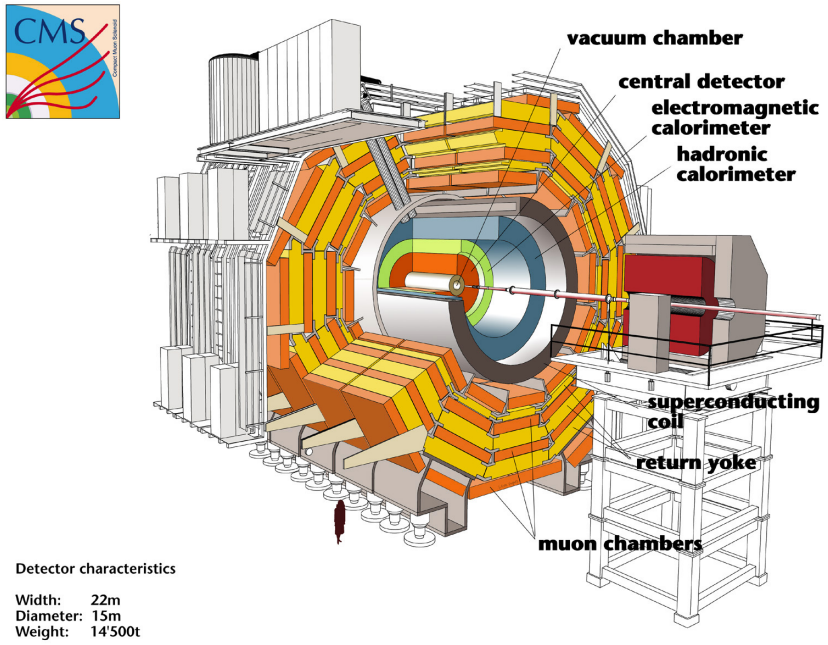


Figure 7 – Illustration of the CMS detector, showing its layered structured with the outer four layers for detecting muons (interleaved with three layers of iron), the central calorimeters and the inner tracking system. From the CERN Document Server. [55]

behaviour in small systems such as pp and pPb collisions are also of great interest, thus being among the main objects of study of the CMS collaboration.

The CMS detector is composed by many sub-detectors that are designed to track, measure or stop different types of particles emerging from the collisions. The general structure of the detector is shown in Figure 7, which highlights the layered structure of the CMS detector, labeling its different sub-detectors.

The closest system to the beam pipe is the silicon tracker, which is designed to provide an efficient measurement of the trajectories of particles emerging from the collisions. It does so by charting the positions of the produced particles in a number of key points. It surrounds the interaction point (IP) and is composed by many barrel layers and endcaps. This design ultimately allows for a tracker acceptance to a pseudorapidity of $|\eta| < 2.5$. The structure and coverage of the tracker is shown in Figure 8. The CMS tracker together with the CMS charged particle reconstruction algorithm (tracking), gives an efficient and precise reconstruction of the trajectories of charged hadrons with transverse momentum above 0.3 GeV [56].

After passing the tracker, the particles reach the electromagnetic calorimeter (ECAL), where the photons and electrons interact with lead tungstate crystals to pro-

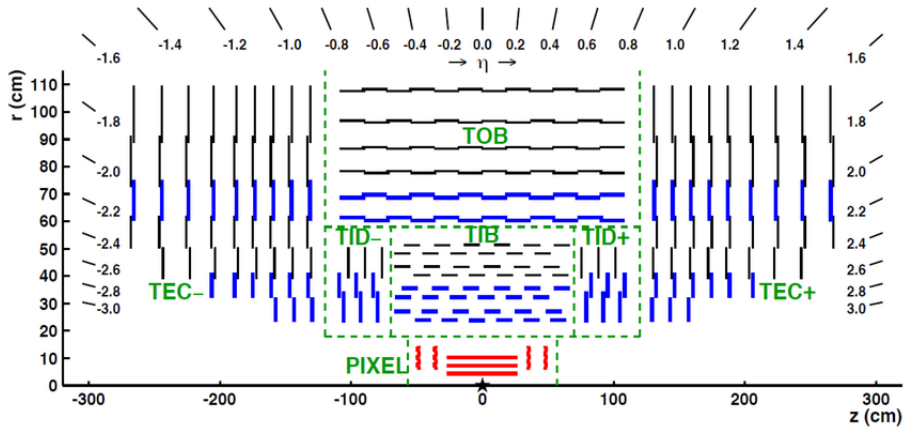


Figure 8 – Schematic view of the upper half of the CMS inner tracker, showing the system basic structure and pseudorapidity (defined below) coverage. [57].

duce radiation proportional to the impinging particle's energy. This allows for a precise measurement of the energy of photons and electrons produced in the collisions and the reconstruction of their tracks. Effectively, all electrons and photons emitted stop at the ECAL.

Moving radially outward, the next layer of the detector is the hadron calorimeter (HCAL), which is designed to accurately measure the energy of all the hadrons produced in the events. To measure the energy of hadrons, the HCAL is constructed with alternating layers of absorber and scintillator materials that produce a light pulse when the particle passes through. Special optic fibres collect up this light and feed it into signal amplifiers. When the amount of light in a given region is summed up over many layers of tiles in depth, called a "tower", this total amount of light is a measure of a particle's energy [49].

The HCAL is organised into barrel (HB and HO), endcap (HE) and forward (HF) sections. There are 36 barrel "wedges" that form the last layer of detector inside the magnet coil. The outer barrel (HO) of the calorimeter is placed outside the coil to ensure no energy is leaked out the back of the HB undetected. Similarly, 36 endcap wedges measure particle energies as they emerge through the ends of the solenoid magnet. Lastly, the two hadronic forward calorimeters (HF) are positioned at either end of CMS, to pick up the bulk of particles coming out of the collision region at shallow angles relative to the beam line. The HF is placed at 11.2 m from the interaction point which ultimately extends the pseudorapidity coverage to $|\eta| = 5.2$, assuring very good hermeticity.

Outside the superconducting coil, three layers of an iron magnet "return yoke" are placed as to filter any remaining particles, effectively allowing only muons and neutrinos to

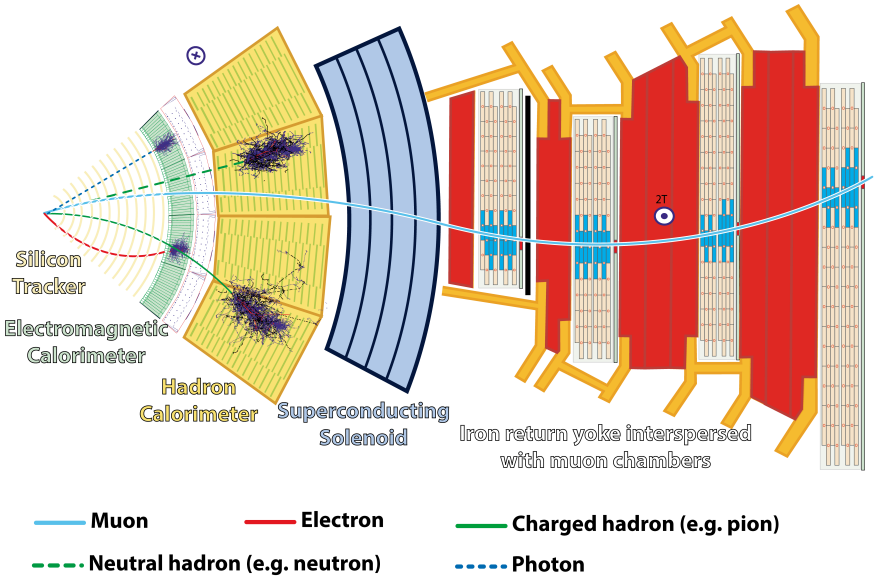


Figure 9 – Transverse slice showing CMS sub-detectors and how different particles interact with them. From the CMS collection. [58]

go through. The muon detector system is composed by four layers of muon chambers that are interleaved with the iron yoke. Figure 9 shows a transverse view of the CMS detector and illustrates how different types of particles interact with its different sub-detectors.

3.3 The CMS coordinate system and collision observables

The CMS uses a right-handed cylindrical coordinate system, centered at the nominal interaction point, as shown in Figure 10. The x-axis points radially inward toward the center of the LHC ring, the y-axis pointing vertically upward, and the z-axis is aligned along the beam direction. This coordinate system is fully characterized by the coordinates θ, ϕ and z, where θ is the polar angle between the particle's momentum vector and the beam axis z, and ϕ is the azimuthal angle measured in the x–y plane with respect to the positive x-axis.

In a particle accelerator, however, the angular position of a particle is more conveniently described by its pseudorapidity η, defined in Eq. 4. The pseudorapidity provides a boost-invariant measure of the polar angle relative to the beam axis, and it essentially tells how forward or how central a particle's trajectory is with respect to the beam. The pseudorapidity is zero in any direction perpendicular to the beam (central region), and it tends to $\pm\infty$ as you get closer to the beam axis. The large $|\eta| > 3$ regions are called forward regions.

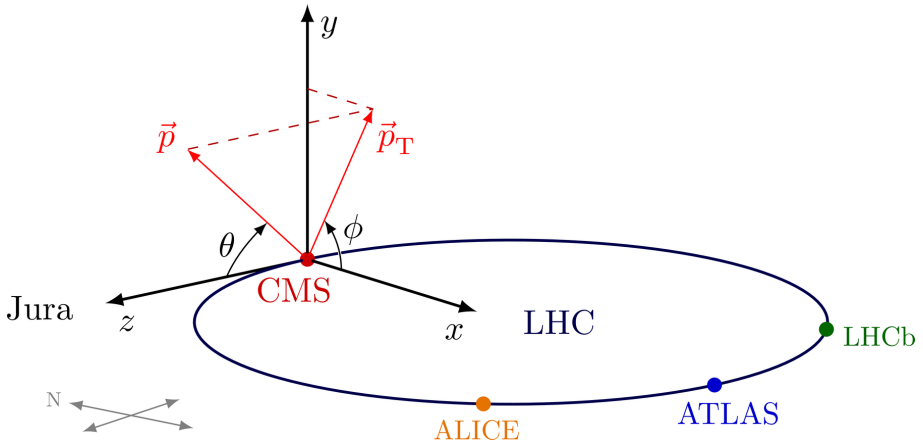


Figure 10 – The CMS coordinate system, including the LHC tunnel and a compass. [59]

In ultra-relativistic pPb collisions at the LHC, the high-energy proton interacts with a lead nucleus boosted in the opposite beam direction within a timescale of order $\sim$ 1fm/c. At the microscopic level, the collision is initiated by multiple parton–parton[4] interactions between quarks and gluons in the proton and in the Pb nucleus. At LHC energies, the parton densities are large, and both soft and hard QCD processes contribute to particle production. Hard scatterings may produce high transverse momentum partons that subsequently fragment into jets, while soft interactions dominate the bulk particle production at low transverse momentum.

In large systems such as PbPb collisions, the energy deposited in the overlap region leads to the formation of a system composed of strongly interacting quarks and gluons. Following this initial energy deposition, the system undergoes rapid longitudinal expansion and cooling. Supposing local thermodynamic equilibrium is approximately achieved, the subsequent evolution of the medium can be described in terms of relativistic hydrodynamics. In smaller systems, such as pPb collisions, the formation of a similar strongly interacting system is still under strong debate in the scientific community. In this work, we assume approximate local equilibrium and explore possible collective signatures through global observables. As the system expands and cools below the confinement temperature, quarks and gluons hadronize and propagate outward, until kinetic freeze-out is reached and their momenta become fixed.

Experimentally, the produced particles are detected through their interactions with the various CMS sub-detectors. The charged hadrons are reconstructed via their

[4] The term “parton” refers to the constituents of hadrons that participate in high-energy interactions. In the framework of quantum chromodynamics (QCD), partons correspond to quarks and gluons inside a hadron.

trajectories in the silicon tracking system, which provides precise measurements of transverse momentum p_{T} and pseudorapidity η. Calorimeters measure the energy deposited by electromagnetic and hadronic showers, allowing the determination of transverse energy and event activity.

The charged-particle multiplicity, denoted by N_{ch}, represents the number of primary charged particles produced in a collision event. As charged particles leave measurable tracks in the tracking detectors, N_{ch} is a directly accessible experimental observable. It provides a quantitative measure of the event activity and is strongly correlated with the underlying collision geometry and the amount of energy deposited in the system.

3.4 Trigger system for data acquisition

The LHC has a nominal bunch-crossing frequency of 40 MHz, corresponding to one bunch-cross every 25 ns. For ultrarelativistic pPb collisions, the interaction rate is approximately 2 MHz, depending on the instantaneous luminosity of the experiment. In any case, each event consists of about 1 MB of data, leading to a nominal raw data production rate of approximately 2 TB/s, far exceeding storage capabilities of the detector [45].

The storage of all the collision data is impractical at real time, and an event-selection filter is implemented in order to reduce the data storage and thus to select only a small but representative subset of events for further processing and analysis. At the CMS experiment, the real-time event-selection is implemented by the CMS trigger system, which consists of a two-level system that performs data selection while still preserving the physical information of the collision experiment.

The two-level architecture of the CMS trigger system consists of a hardware-based Level-1 (L1) trigger followed by a software-based High-Level Trigger (HLT). The L1 trigger consists of custom-designed programmable electronics responsible for reducing the event-selection rate to ~ 100 kHz, which matches the capability of the CMS data acquisition system. The L1 trigger selects events based on energy deposits in the ECAL, HCAL and HF calorimeters, as well as information from the muon detectors. Events accepted by the L1 trigger are further processed by the HLT, which runs software algorithms to reduce the input event rate of 100 kHz to an output rate of 1 kHz of events that are ultimately written to permanent storage. The HLT performs data selection based on information

from the tracking system, performing cuts on p_{T} of reconstructed tracks, track–calorimeter matching and vertex and multiplicity requirements [60]. The particular set of triggers used for data-selection depends on each experiment. The set triggers used for the data sample analyzed here is described in Chapter 4.

4 Measurement methodology and data analysis framework

The main goal of this work was to study the correlation between $\langle p_{\mathrm{T}} \rangle$ and N_{ch} in pPb collision data at $\sqrt{s_{\mathrm{NN}}} = 5.02$ TeV and $\sqrt{s_{\mathrm{NN}}} = 8.16$ TeV collected by the CMS. In particular, the study of this correlation at two different collision energies allow the calculation of the speed of sound squared c_s^2 in the system created in ultrarelativistic pPb collisions, given that one defines an effective temperature for the system T_{eff} based on the average transverse momentum of the final-state particles. In this Chapter, the methodology implemented in this work is described in detail. First, the set of triggers used by the CMS for online and offline event reconstructions is described. Quality assurance plots are presented as they constitute the first step of any data analysis. The ROOT data objects such as histogram distributions for track and event-level observables are described. The transverse momentum distributions are classified according to the event activity, in order to control event fluctuations and to allow for an analysis within each centrality bin. To correct for detector acceptance bias, the transverse momentum distribution of the reconstructed tracks is extrapolated to the $p_{\mathrm{T}} > 0$ GeV region. Systematic uncertainties are not calculated in this work, although a brief section is given about the required steps to calculate it.

4.1 Online and offline event selections

This analysis uses proton–lead (pPb) collision data collected in 2016 by the CMS experiment at the CERN-LHC, corresponding to an integrated luminosity of 186 nb^{-1} at $\sqrt{s_{\mathrm{NN}}} = 8.16$ TeV and 0.509 nb^{-1} at $\sqrt{s_{\mathrm{NN}}} = 5.02$ TeV.

The pPb datasets were collected with minimum-bias (MB) triggers designed to select inelastic hadronic pPb interactions with high efficiency and minimal bias. MB events are collisions selected with minimal trigger requirements, intended to represent as closely as possible the inclusive inelastic interaction sample. These collisions correspond to events that are not biased toward rare processes such as high transverse momentum production (high p_{T} jets) or large energy deposition. Therefore, a MB event sample contains predominantly soft QCD interactions and reflects the typical particle production characteristics of the collision system. Thus, MB triggers provide the most representative

dataset for analyzing global observables such as charged-particle multiplicity N_{ch} and mean transverse momentum $\langle p_{\mathrm{T}} \rangle$.

For both collision energies, the trigger strategy followed the standard CMS heavy-ion approach, using forward calorimetry triggers at Level-1 (L1), followed by tracking requirements at the High-Level Trigger (HLT). At the L1 stage, the minimum bias events are triggered by requiring energy deposits above 1 GeV in at least one of the two HF calorimeters. At the HLT level, the minimum-bias triggers required at least one online reconstructed track with $p_{\mathrm{T}} > 0.4$ GeV using hits from only the pixel tracker.

The efficiency of the minimum-bias triggers was studied using zero-bias data [1] and Monte Carlo (MC) simulations [61]. For both collision energies, the trigger efficiency is found to be close to 100% for events with at least one reconstructed track above $p_{\mathrm{T}} > 0.4$ GeV, and remains above approximately 95% when integrated over all inelastic hadronic pPb events.

In addition to the minimum-bias triggers, dedicated high-multiplicity (HM) triggers were employed to enhance the sample of events with large charged-particle multiplicities. These triggers are designed to efficiently select rare, high-activity pPb collisions that are particularly relevant for studies of collective phenomena. The high-multiplicity trigger strategy is built upon the minimum-bias selection at the L1 stage and applies additional requirements only at the HLT stage based on the number of reconstructed pixel tracks, including a transverse momentum threshold of $p_{\mathrm{T}} > 0.4$ GeV and a pseudorapidity acceptance of $|\eta| < 2.4$. Several HM triggers are defined by applying progressively higher thresholds on the number of reconstructed pixel tracks, $N_{\mathrm{trk}}^{\mathrm{online}}$, thereby selecting event classes corresponding to increasing event activity. By imposing progressively higher thresholds on $N_{\mathrm{trk}}^{\mathrm{online}}$, HM triggers provide access to regions of phase space that would otherwise be statistically limited in minimum-bias data alone.

After online selection, a set of offline event-quality criteria was applied to ensure a clean sample of hadronic pPb collisions. A reconstructed primary vertex is required within $|v_z| < 15$ cm of the nominal interaction point, with at least two associated tracks. Events contaminated by beam-related backgrounds, such as beam scraping or beam–gas interactions, are rejected using dedicated filters based on track quality and vertex properties. In particular, events with a large number of reconstructed tracks but a low fraction of high-purity tracks are removed. A cutoff on the significances $|\mathrm{d}xy|/\sigma_{\mathrm{d}xy} < 3.0$ and $|\mathrm{d}z|/\sigma_{\mathrm{d}z} < 3.0$

[1]

was applied in order to keep only primary tracks and reduce contributions from secondary vertices.

To suppress electromagnetic interactions from ultra-peripheral events (UPC), a coincidence requirement in the HF calorimeters is imposed offline. This requires at least one HF tower on each side of the detector with an energy deposit above 3 GeV. This requirement removes approximately 99% of UPC events.

Although the pileup probability in pPb collisions is significantly lower than in pp running, it is not negligible, particularly for the 8.16 TeV data, where higher instantaneous luminosities were achieved. Pileup effects are mitigated by applying dedicated vertex-based pileup filters that reject events with multiple interaction vertices too close to each other along the beam axis.

The nominal pileup filter used in this analysis is the overlapping-vertex filter, which removes events containing additional vertices within a small distance from the primary vertex, with thresholds that depend on the number of tracks associated with the secondary vertices. This approach efficiently suppresses pileup while preserving more than 99% of genuine single-collision events. Alternative pileup filters were used in systematic studies to assess the associated uncertainties.

It is important to mention that in pPb collisions, the unequal beam energies per nucleon result in a longitudinal boost of the nucleon–nucleon center-of-mass frame with respect to the laboratory frame, unlike symmetric systems like pp or PbPb. The CM in pPb collisions is shifted towards the proton beam direction, with a rapidity shift of $y_{\mathrm{CM}} = 0.465$ for both collision energies [62]. The beam-direction reversal is thus employed to mitigate and control potential detector asymmetries with respect to the rapidity. The data taking for pPb collisions was divided into two periods, with the direction of each colliding beam reversed after the first period.

The trigger strategy and event selection described above provide a high-purity and well-controlled sample of pPb collisions datasets, enabling a consistent comparison of observables across collision energies and multiplicity classes.

The data was stored using ROOT, an open-source software package developed at CERN [63] which provides a very efficient data storage system as well as processing and analysis of scientific data. ROOT is delivered with a C++ interpreter and it is widely used from data acquisition to data analysis and visualization.

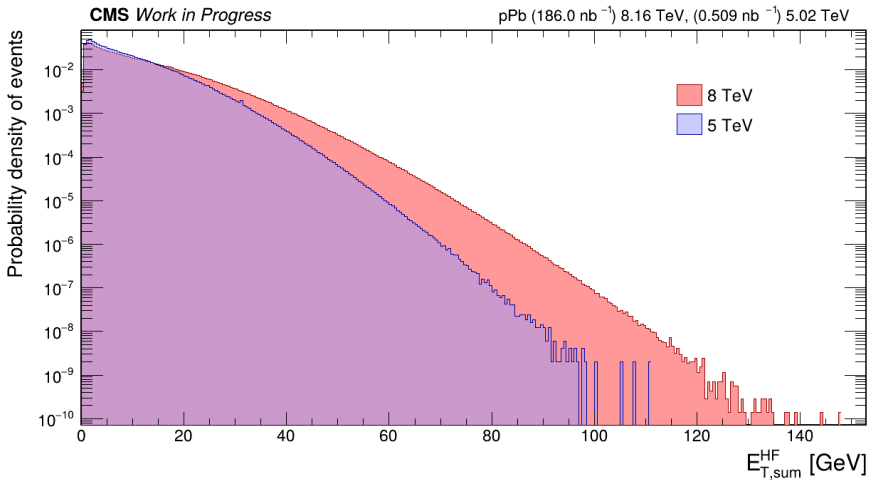


Figure 11 – Sum of the transverse energy deposited in the HF calorimeter $E^{\mathrm{HF}}_{\mathrm{T,sum}}$ on the side of the detector facing the outgoing Pb beam.

4.2 Control plots

The control plots represent the first step of a data analysis of high-energy heavy-ion collisions, since they verify the consistency of the data with the set of triggers used, and both online and offline reconstruction, ultimately aiming to establish confidence for further steps of the analysis and calculations. In this work, the quality-assurance histograms are made for track-level quantities such as reconstructed p_{T}, η and ϕ distributions, as well as event-level quantities such as the position of the reconstructed primary vertex along the z–axis v_z and the sum of the transverse energy deposited on the HF calorimeters $E^{\mathrm{HF}}_{\mathrm{T,sum}}$.

Figure 11 shows the distribution of the sum of the transverse energy deposited in the hadronic forward calorimeter $E^{\mathrm{HF}}_{\mathrm{T,sum}}$ on the side of the detector facing the outgoing lead (Pb) beam. The HF calorimeters cover the forward pseudorapidity region $2.9 < \eta < 5.2$ and thus are particularly correlated to event activity.

The observed distribution for $E^{\mathrm{HF}}_{\mathrm{T,sum}}$ exhibits a smooth, monotonically decreasing shape, with a large population at low transverse energy and a progressively smaller number of events at higher values. This behavior is expected for inelastic pPb collisions and reflects the broad range of event activity sampled by the minimum-bias and high-multiplicity triggers. The absence of anomalous structures or sharp features indicates a stable detector response and confirms that the event selection does not introduce artificial biases in the forward energy measurement.

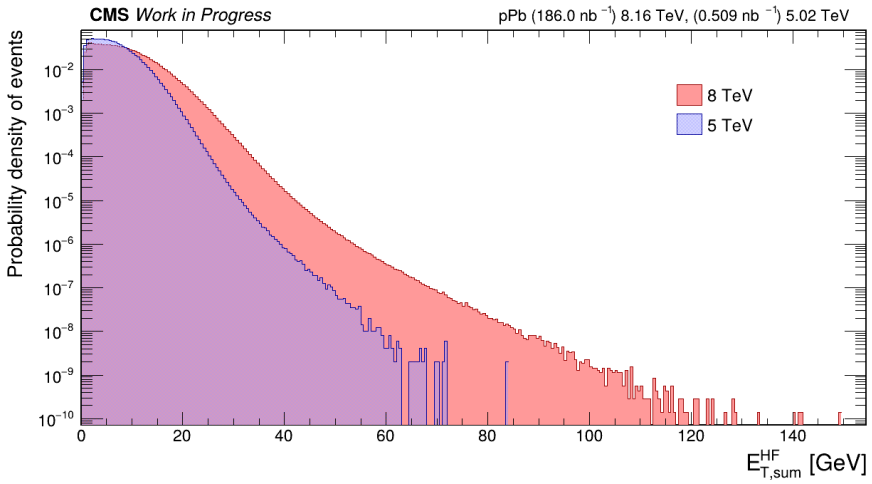


Figure 12 – Sum of the transverse energy deposited on the proton-going side of the HF detector.

The distribution for the sum of the transverse energy deposited on the proton-going side of the HF detector is shown in Figure 12. Due to the asymmetric nature of pPb collisions, the transverse energy deposited on the proton-going side is generally lower than on the Pb-going side, reflecting the smaller number of participating nucleons from the proton beam. The control plot shows a distribution consistent with this expectation, characterized by lower overall transverse energy compared to the Pb-going side and a smooth fall-off toward higher values. The agreement between the qualitative shape of this distribution and known pPb collision trends confirms that the forward calorimeters are functioning properly and that the beam-direction assignment has been correctly implemented in the analysis.

Another event-level quantity that is commonly checked in quality-assuring histograms is the longitudinal position of the reconstructed primary vertex along the beam axis v_z, measured relative to the nominal interaction point of the CMS detector. The distribution of v_z is shown in Figure 13. The distribution is centered around zero and exhibits a symmetric shape consistent with the expected longitudinal beam profile. The absence of distortions or secondary peaks indicates that non-collision backgrounds and beam–gas interactions have been effectively suppressed. Furthermore, the threshold value of $|v_z| < 15$ cm used in the offline track selection is apparent in the plot. This cut is applied mainly to avoid detector acceptance effects on the analysis (for example, a significant part of a charged particle trajectory being outside the region covered by detector modules).

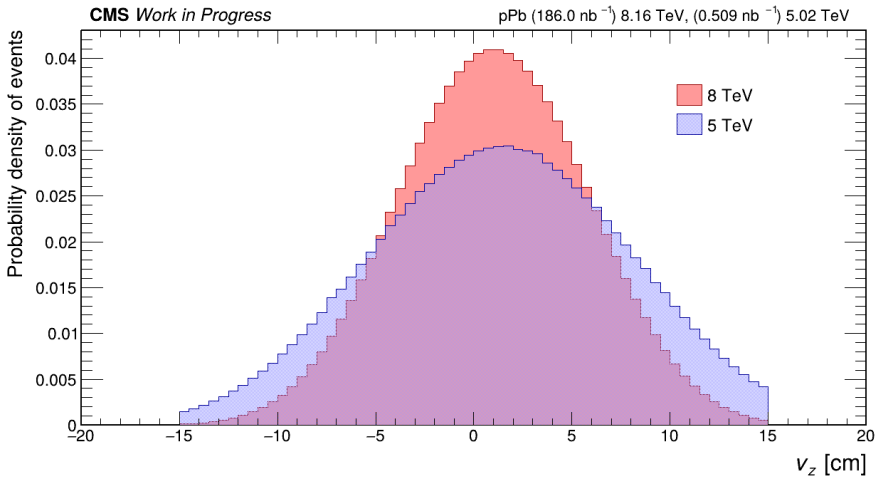


Figure 13 – Longitudinal position of the reconstructed primary vertex along the beam axis v_z, measured relative to the nominal interaction point of the CMS detector.

Moreover, the broader v_z distribution observed in the 5.02 TeV pPb dataset compared to 8.16 TeV can originate from differences in LHC beam optics and longitudinal bunch profiles between the two running periods. Nevertheless, the gaussian profile is clearly seen for both datasets which ultimately ensure data consistency.

Quality-assurance plots for track-level quantities are also analyzed. The transverse impact parameter significance $\mathrm{d}xy/\sigma_{\mathrm{d}xy}$ is defined as the transverse distance of closest approach of a track to the primary vertex in the plane perpendicular to the beam, divided by its associated uncertainty. This variable is most important as to distinguish between tracks originating from the primary collision and secondary tracks arising from decays of long-lived particles, interactions with detector material, or misreconstructed tracks.

The distribution of $\mathrm{d}xy/\sigma_{\mathrm{d}xy}$ is shown in Figure 14. The distribution is sharply peaked around zero and approximately symmetric, as expected for emitted charged particles produced at the primary vertex. The observed gaussian profile with thresholds consistent with those used in the offline data-selection confirms the good quality of the track reconstruction and the effectiveness of the track selection criteria.

The longitudinal impact parameter significance $\mathrm{d}z/\sigma_{\mathrm{d}z}$, on the other hand, measures the displacement of a reconstructed track relative to the primary vertex along the beam direction, normalized by its uncertainty. Like its transverse counterpart, this observable probes the consistency of reconstructed tracks with the primary vertex and is sensitive to pileup and secondary contributions.

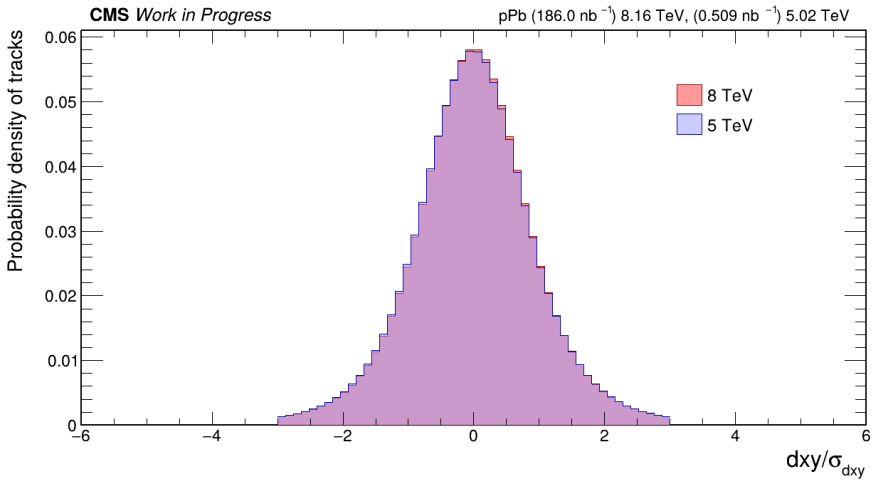


Figure 14 – Distribution of transverse impact parameter significance $\mathrm{d}xy/\sigma_{\mathrm{d}xy}$ of reconstructed tracks.

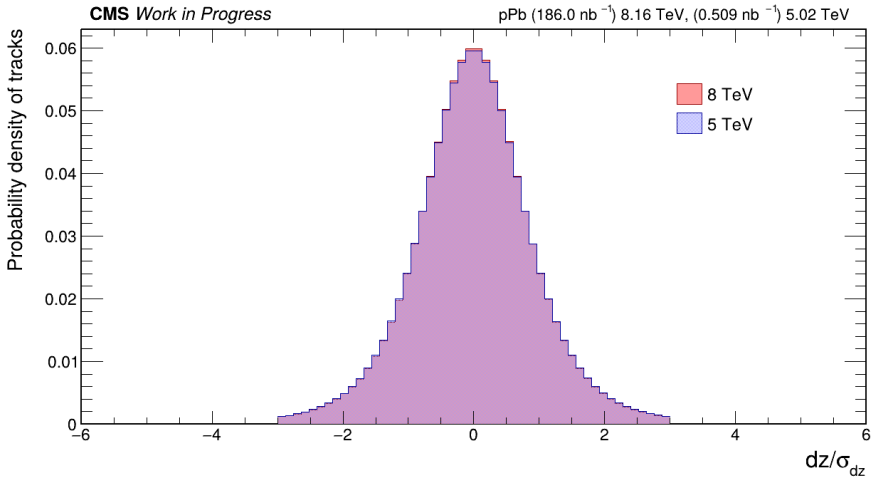


Figure 15 – Distribution for longitudinal impact parameter significance $\mathrm{d}z/\sigma_{\mathrm{d}z}$ of reconstructed tracks.

The control plot for $\mathrm{d}z/\sigma_{\mathrm{d}z}$ of Figure 15 shows a narrow distribution centered at zero, indicating that the majority of selected tracks originate from the reconstructed primary vertex. The gaussian profile of the distribution again demonstrates good vertex resolution and effective pileup rejection, supporting the reliability of the reconstructed track sample used in the analysis.

The transverse momentum p_{T} distribution of reconstructed charged particles can reflect the dynamics of particle production as well as the performance of the tracking system. Figure 16 shows the control plot for the p_{T} distribution of reconstructed tracks in the pPb collisions. The observed trend is a steeply falling distribution toward higher transverse momenta, with a large population of low-p_{T} tracks, indicating that pPb collisions are predominantly characterized by soft interactions. The observed shape is characteristic

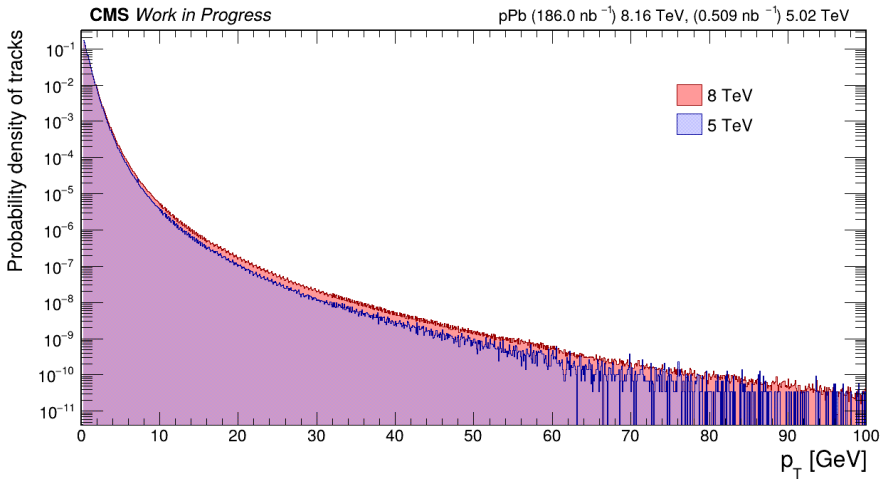


Figure 16 – Transverse momentum p_{T} distribution of reconstructed charged particles.

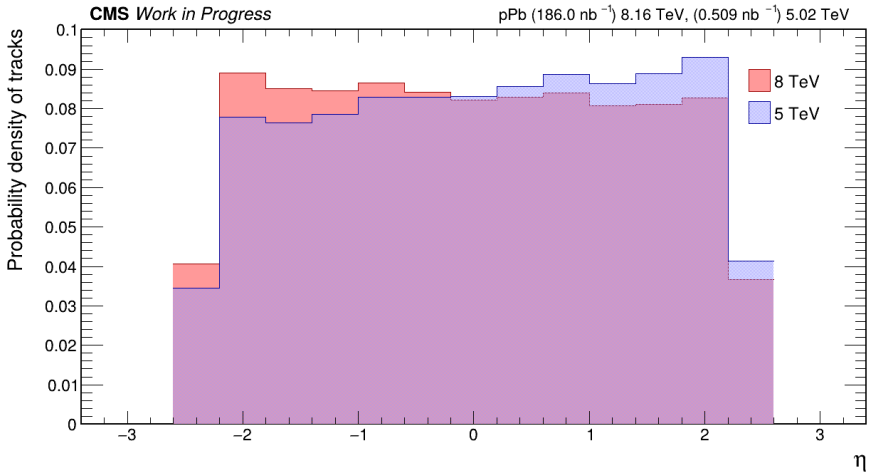


Figure 17 – Pseudorapidity η distribution for reconstructed tracks.

of minimum-bias samples and indicate that the reconstruction and selection criteria do not introduce artificial distortions in the momentum spectrum. At high transverse momentum, the charged-particle yield falls greatly. As a result, the tail of the p_{T} distribution is populated by very few tracks, making it highly sensitive to statistical fluctuations.

The pseudorapidity η distribution of reconstructed tracks was also analyzed as a quality assurance plot, as it reflects the detector acceptance and the longitudinal dynamics of the collision system. Figure 17 shows the η distribution of reconstructed tracks for both collision energy datasets of pPb collisions. The asymmetry observed in the distribution is due to the intrinsic asymmetry of the proton–lead system, since the proton and lead nuclei carry different energies per nucleon and produce different particle densities, a resulting particle production asymmetry in pseudorapidity regions is seen.

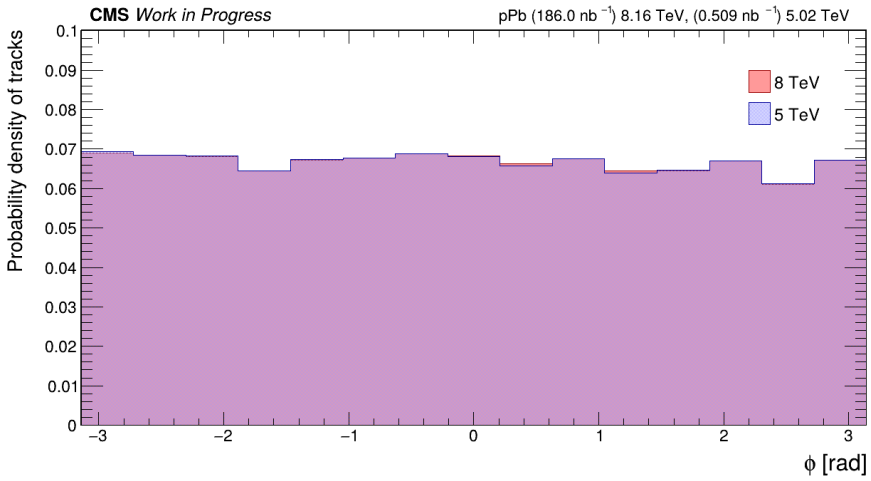


Figure 18 – Azimuthal angle ϕ distribution of reconstructed tracks.

Finally, the azimuthal angle ϕ distribution of reconstructed charged-particle tracks is shown in Figure 18. Since the CMS detector is approximately azimuthally symmetric and the event sample used in this analysis does not impose any selection bias in ϕ, the expected distribution is uniform over the full azimuthal range. The observed distribution is indeed consistent with a flat behavior within statistical uncertainties for both collision energies, indicating the absence of detector-induced asymmetries or reconstruction artifacts in the azimuthal direction. The close agreement between the 5.02 TeV and 8.16 TeV data further demonstrates that the tracking performance and acceptance are stable across different running conditions.

4.3 Centrality estimation

In high-energy nuclear collisions, the concept of centrality is used to characterize the geometry of the interaction. More intuitively, centrality is related to the impact parameter b, defined as the transverse distance between the centers of the two colliding nuclei at the moment of closest approach. Collisions with small impact parameter ($b \approx 0$) are referred to as central collisions and correspond to a large overlap region between the nuclei, leading to a high number of participating nucleons and a large particle multiplicity. Conversely, collisions with large impact parameter are called peripheral and involve a smaller overlap region, fewer participating nucleons, and lower multiplicity. Figure 19 illustrates a PbPb collision reconstructed at the LHC with $b \approx 7$. Number of participants are counted by

nucleons that collide with any nucleon, whereas the number of binary collisions count all overlapping blue/red nucleon pairs.

Since the impact parameter b cannot be measured directly in experiments, centrality classes are defined using experimentally accessible observables which are monotonically correlated with b through geometric models such as the Glauber model [64], allowing events to be categorized into percentiles that reflect the fraction of the total inelastic cross section. This procedure groups together events with similar overall activity, enabling a controlled study of how observables evolve as a function of event activity rather than being dominated by trivial averaging effects.

In pPb collisions, particle production exhibits large event-by-event fluctuations, even at fixed center-of-mass energy. These fluctuations arise from several sources, including variations in the number of participating nucleons in the lead nucleus and fluctuations coming from partonic distribution functions substructure. As a result, minimum-bias pPb data represent an ensemble of collision events with vastly different final-state particle densities and effective system sizes. For bulk observables that are sensitive to the global properties of the systems such as the mean transverse momentum $\langle p_{\mathrm{T}} \rangle$, this means averaging over the entire data sample can hide interesting physical trends that depend on event activity. In particular, any dependence of the observable on the overall number of participants or initial entropy density is washed out by the mixing of low-activity and rare high-activity events.

In symmetric heavy-ion collisions such as PbPb, centrality is closely related to the collision geometry and can be approximately mapped to the impact parameter b and the number of participating nucleons [65]. In pPb collisions, however, the intrinsic asymmetry of the system prevents any straightforward geometric interpretation [66]

The proton contains a single participating nucleon, while the lead nucleus can contribute a variable number of nucleons depending on the collision configuration. Consequently, centrality in pPb collisions cannot be interpreted as a direct measurement of the impact parameter. Instead, it needs to be interpreted as an event activity estimator, providing a means to categorize events according to their overall particle production or final-state multiplicity.

In this analysis, the event activity is estimated using the sum of the transverse component of the total energy of the collision $E_{\mathrm{T,sum}}^{\mathrm{HF}}$ deposited in the hadronic forward calorimeter (HF) on the lead-going (Pb-going) side. This choice addresses the asymmetry

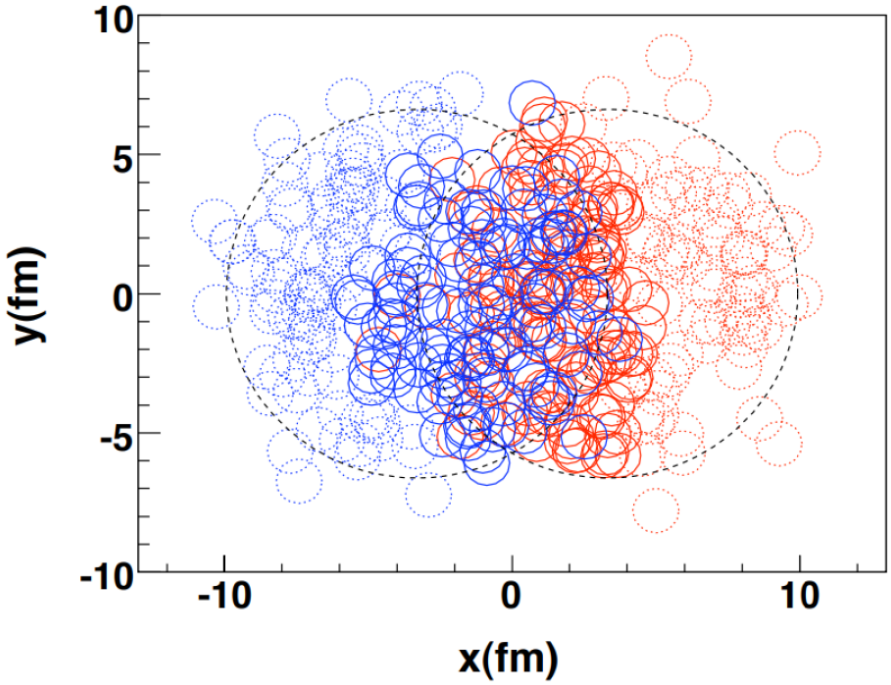


Figure 19 – PbPb collision at LHC with impact parameter $b \approx 7$ fm. Number of participants (solid) are counted by nucleons that collide with any nucleon, whereas the number of binary collisions count all overlapping blue/red nucleon pairs. Spectators (dashed) do not collide. Adapted from [3].

of the pPb system, in which particle production in the Pb fragmentation region is more strongly correlated with the number of participating nucleons and thus with the overall event activity. The proton-going (p-going) side is reportedly more dominated by fluctuations from a single interacting nucleon, exhibits larger event-by-event fluctuations and a weaker correlation with collision geometry. Furthermore, using only the Pb-going side maximizes the rapidity separation between the event activity estimator and midrapidity observables, thereby reducing auto-correlation effects [40]. For example, hard processes originating early in the collision tend to fragment into large numbers of high-p_{T} particles, yet these particles may not reflect an increase in the entropy profile and temperature of the QGP medium. For these reasons, the Pb-going HF energy provides a more robust and less biased event activity classification.

In this analysis, three representative centrality classes are used. Namely, the events are classified into 30–80%, 1–30%, and 0–1% centrality bins based on threshold values for $E_{\mathrm{T,sum}}^{\mathrm{HF}}$, calculated previsouly by the CMS collaboration for the data samples. The centrality bin and corresponding $E_{\mathrm{T,sum}}^{\mathrm{HF}}$ thresholds for both pPb datasets are exposed in Table 1.

Table 1 – Centrality and corresponding $E_{\mathrm{T,sum}}^{\mathrm{HF}}$ threshold values for the pPb data samples.

Centrality	$E_{\mathrm{T,sum}}^{\mathrm{HF}}$ **(5.02 TeV)**	$E_{\mathrm{T,sum}}^{\mathrm{HF}}$ **(8.16 TeV)**
30–80%	2.5–11.5 GeV	2.5–14.5 GeV
1–30%	11.5–35 GeV	14.5–44 GeV
0–1%	$>$ 35 GeV	$>$ 44 GeV

The 30–80% centrality class corresponds to events in the lowest activity region of the selected sample. These events are characterized by low particle multiplicity and small energy deposition in the Pb-going HF. The 1–30% centrality class represents events with significantly enhanced particle production relative to minimum-bias collisions. This region probes events in which multiple nucleons in the lead nucleus participate, making it a natural transition region for studying the emergence of collective behavior. The 0–1% centrality class corresponds to the highest-activity pPb events and is of particular interest for small-system studies.

The pPb collision data samples were stored in specific ROOT data storage formats, which correlates the track-level quantities like p_{T} and η with event-level quantities such as the $E_{\mathrm{T,sum}}^{\mathrm{HF}}$. This allows the CMS to bin these observables into three-dimensional histograms that allow the study of the correlation between $\langle p_{\mathrm{T}} \rangle$, η and $E_{\mathrm{T,sum}}^{\mathrm{HF}}$. The events are classified in the different centrality bins according to such a histogram. In this analysis, we select the pseudorapidity window $|\eta| < 1.5$ and thus integrate the three-dimensional histogram from $\eta_1 = -1.5$ to $\eta_2 = 1.5$ into a two-dimensional histogram binned according to the transverse momentum of reconstructed tracks and their respective $E_{\mathrm{T,sum}}^{\mathrm{HF}}$. This histogram is shown in Figure 20, with the palette indicating the number of tracks in each bin. The centrality classification is illustrated in the figure, where vertical lines indicate the different centrality samples over the histogram.

4.4 Fit and extrapolation of p_T spectrum

The CMS tracking system together with the reconstruction algorithm are able to reconstruct charged particles with reasonable efficiency (above 50%) and low fake rate (below 2%) for $p_{\mathrm{T}} > 0.3$ GeV. However, the real p_T spectrum of the produced particles is for $p_{\mathrm{T}} > 0$ GeV. Thus, in order to account for detector limitations and bias, an extrapolation of the CMS data to the $p_{\mathrm{T}} < 0.3$ GeV region is necessary.

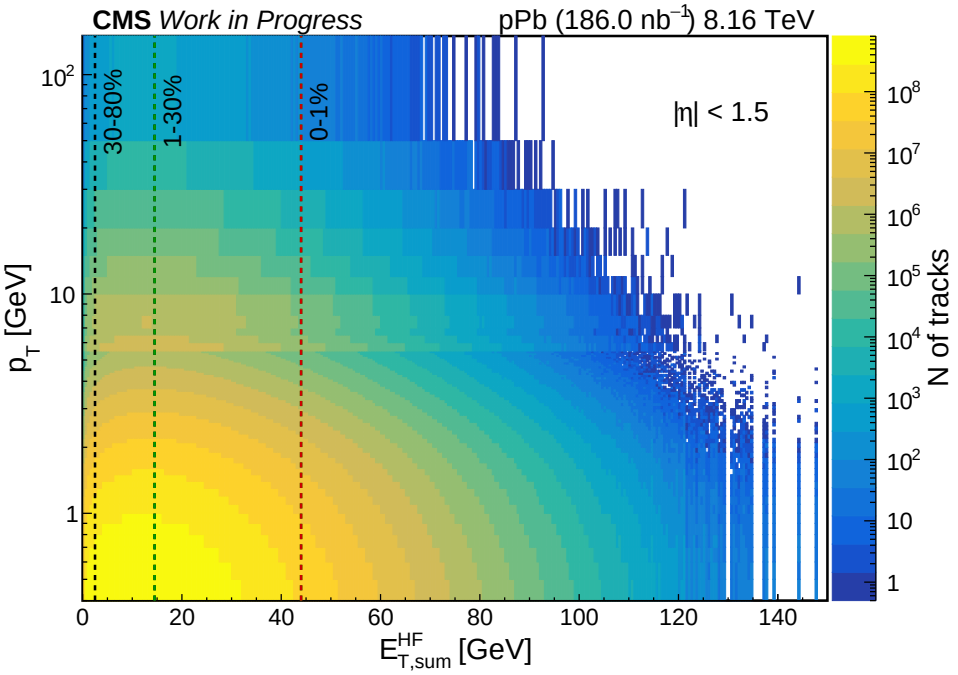


Figure 20 – The sample of all events is classified in centrality bins of similar event activity. The graph shows the relative size of each sample for the case of $\sqrt{s_{\rm NN}} = 8.16$ TeV on the pseudorapidity window $|\eta| < 1.5$. The vertical lines indicate threshold values for $E^{\rm HF}_{\rm T,sum}$ indicated in Table 1. The same binning applies to the 5.02 TeV case with its respective threshold values.

In the present work we perform such an extrapolation in two steps. First, we fit the CMS data for $p_{\rm T} > 0.3$ GeV over the interval $[0.3, 1.5]$ GeV using a Hagedorn function [67, 68] defined by

$$\frac{dN_{\rm ch}}{dp_{\rm T}} = A\, p_{\rm T} \left(1 + \frac{1}{\sqrt{1-\langle\beta_T\rangle^2}} \frac{\sqrt{p_{\rm T}^2 + m_\pi^2} - \langle\beta_T\rangle p_{\rm T}}{n\,T} \right)^{-n} . \tag{13}$$

This function has five parameters. The pion mass is fixed at the value $m_\pi = 0.13957$ GeV [69]. The temperature T at the kinetic freeze-out is set to optimization in the interval $[0.0, 0.5]$ GeV. The $\langle\beta_T\rangle$ parameter is related to the radial flow velocity in the system, and has fixed values for each collision energy. In this work, we use $\langle\beta_T\rangle(5.02\ \text{TeV}) = 0.4034$ and $\langle\beta_T\rangle(8.16\ \text{TeV}) = 0.5010$ (obtained by checking in the ALICE pPb data spectrum starting at $p_{\rm T} = 0.15$ GeV, which parameter values provide the best fit for $p_{\rm T} > 0.3$ GeV to extrapolate the spectrum down to $p_{\rm T} = 0.15$ GeV). The amplitude A of the function needs to represent the magnitude of the track sample, and thus an initial value is set as 7.5×10^9, with freedom for optimization. The parameter n has no physical

meaning in the context of this work and its value is free for optimization in the interval $[6.0, 9.0]$.

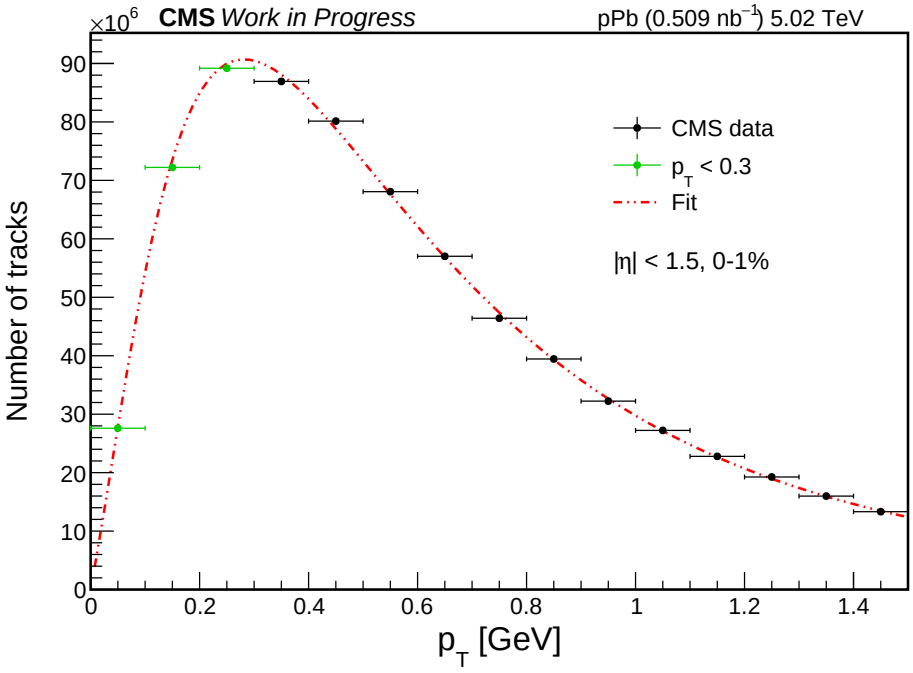
This configuration for the Hagedorn function is effectively fitted to the CMS data for both the 5.02 TeV and 8.16 TeV datasets. Once the parameters are fit to the track p_{T} distribution data for each collision energy, a new histogram is filled using a probability distribution function associated with the Hagedorn Equation 13. This is done by generating random events with ROOT's random generator that follow the Hagedorn-fitted probability distribution on the interval $[0.0, 1.5]$ GeV on the condition that the number of tracks on the $[0.3, 1.5]$ GeV region should be the same for both extrapolated and observed data. The generated tracks that fall on the interval $p_{\mathrm{T}} \in [0.0, 0.3]$ GeV are used to extrapolate the CMS data on a final histogram with $p_{\mathrm{T}} > 0$ GeV. The bulk observables are finally calculated using this $p_{\mathrm{T}} > 0$ GeV histogram.

The results for the fit of the Hagedorn function from Equation 13 over the $p_{\mathrm{T}} > 0.3$ GeV CMS data for the 0–1% centrality class are shown in Figures 21a and 21b, along with extrapolated data for the p_{T} spectra. The data points correspond to the observed track yield within the experimentally accessible p_{T} range. The spectrum exhibits the characteristic steeply falling behavior expected in pPb collisions, reflecting the dominance of soft particle production at low transverse momentum and a gradual suppression towards higher p_{T}. In both cases, the fitting using Equation 13 shows good agreement with the CMS data. The fit results for the other centrality bins show the same agreement. The extrapolated portion of the p_{T} spectrum is shown in a different color to illustrate the extension of the CMS measured data.

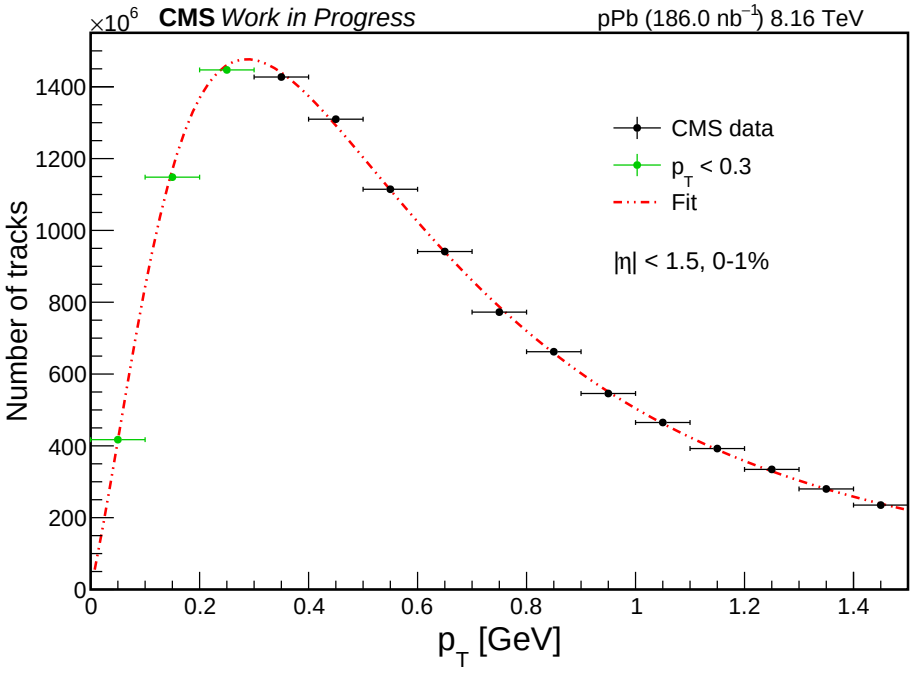
While the extrapolation allows for the subsequent calculation of integrated quantities over the full p_{T} range, it relies on the assumed functional form of Equation 13 and is therefore subject to systematic uncertainties. Nevertheless, the good agreement between the fitted function and the measured data in the accessible region by the CMS supports the validity of the extrapolation within the scope of this analysis.

4.5 Assessing the correlation between $\langle p_T \rangle$ and N_{ch}

As discussed in Section 2.3, the analysis of charged-particle p_{T} distributions in pPb collisions at two different collision energies allows for the study of the thermodynamic



(a) 5.02 TeV



(b) 8.16 TeV

Figure 21 – Results for the fit using a Hagedorn function over the p_T distribution measured by the CMS for the 1% most central pPb collisions. Results are shown for (a) 5.02 TeV and 8.16 TeV. The extrapolated data for $p_T > 0$ is also shown.

properties of the system formed after the collision. In particular, under conditions of approximate local thermal equilibrium, the speed-of-sound squared c_s^2 can be calculated using bulk observables according to

$$c_s^2 = \frac{d\ln\langle p_{\mathrm{T}}\rangle}{d\ln N_{\mathrm{ch}}}. \tag{14}$$

This method used to extract c_s^2 is based on the approach first proposed by Gardim et. al [7], which further motivated similar calculations for c_s^2 in pPb and PbPb systems [41, 54]. In this picture, the bulk observables $\langle p_{\mathrm{T}}\rangle$ and N_{ch} are used as proxies for the thermodynamic properties of the system created in high-energy heavy-ion collisions.

The central assumption of the method is that, for a fixed collision geometry, the effective volume of the produced system remains approximately constant, while changes in collision energy primarily modify the temperature and entropy density of the system. Under this assumption, variations in the average transverse momentum $\langle p_T\rangle$ and the charged-particle multiplicity N_{ch} can be interpreted as reflecting changes in thermodynamic quantities at fixed volume, allowing access to the equation of state through the speed of sound.

To ensure comparable system volumes at different collision energies, the analysis of the correlation $\langle p_{\mathrm{T}}\rangle(N_{\mathrm{ch}})$ is performed within identical centrality intervals. As previously discussed, centrality is defined using the total transverse energy deposited in the HF calorimeters $E_{\mathrm{T,sum}}^{\mathrm{HF}}$. Although the numerical $E_{\mathrm{T,sum}}^{\mathrm{HF}}$ ranges differ between energies, this procedure is designed to select systems with similar initial geometries [7].

The validity of this assumption is supported by simulations performed with the Trajectum model [70], which compare the root-mean-square (RMS) transverse size of the initial system and the number of participant nucleons as functions of centrality at the two collision energies. These studies show that, for the selected centrality classes, both the system size and the number of participants are compatible within uncertainties, justifying the interpretation of the selected events as having comparable effective volumes.

Therefore, we calculate the mean transverse momentum $\langle p_{\mathrm{T}}\rangle$ for each centrality bin, in the pseudorapidity window $|\eta| < 1.5$, using the resulting p_{T} distribution from integrating the two-dimensional histogram of Figure 20 using the $E_{\mathrm{T,sum}}^{\mathrm{HF}}$ threshold values listed in Table 1. The pseudorapidity window $|\eta| < 1.5$ was optimized to ensure high tracking efficiency and low fake-rate.

Within this methodology, the correlation between the average transverse momentum $\langle p_T\rangle$ and the charged-particle multiplicity N_{ch} is presented in Figure 22. A clear and monotonic increase of $\langle p_{\mathrm{T}}\rangle$ with multiplicity is observed in the data at both 5.02 and 8.16

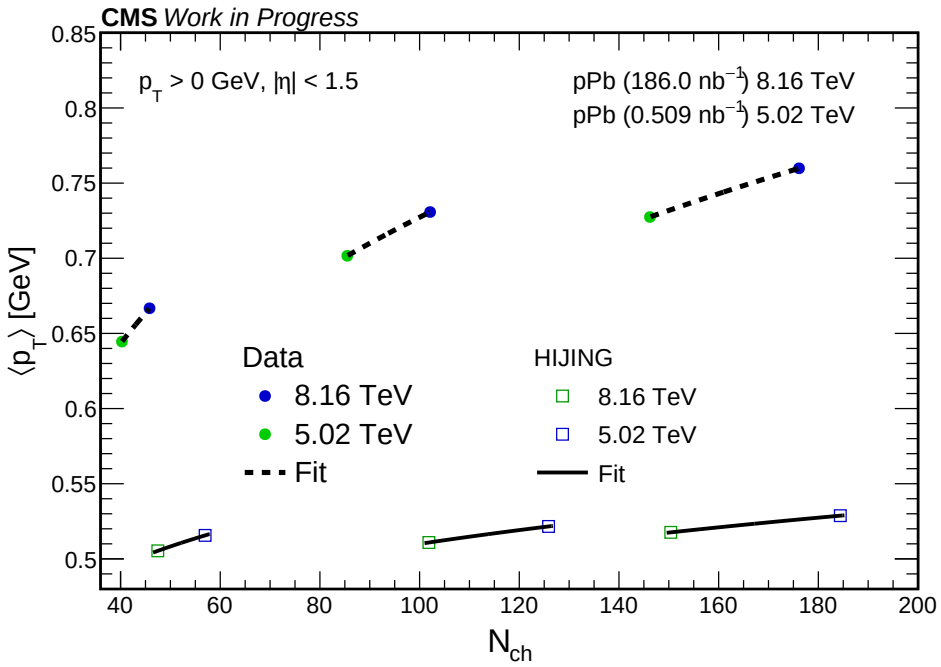


Figure 22 – Correlation between $\langle p_{\mathrm{T}} \rangle$ of the reconstructed tracks, as a function of charged-particle multiplicity N_{ch}. A fit for equivalent centrality classes is performed using the function $\langle p_{\mathrm{T}} \rangle = C N_{\mathrm{ch}}^{c_s^2}$ in order to evaluate the speed-of-sound.

TeV. For each centrality class, the values of $\langle p_{\mathrm{T}} \rangle$ and N_{ch} are measured at each collision energy. The two resulting points corresponding to the same centrality class are then fitted using the integral form of Equation 14. For comparison, predictions from the HIJING event generator are also shown. While HIJING exhibits a mild increase of $\langle p_{\mathrm{T}} \rangle$ with N_{ch}, it systematically underestimates the magnitude of $\langle p_{\mathrm{T}} \rangle$ and fails to reproduce the slope observed in the data. The quantitative results obtained for $\langle p_{\mathrm{T}} \rangle$ and N_{ch} for each centrality class and collision energy is given on Tables 2 and 3 of the Appendix A.

To calculate c_s^2 from the assessed correlation, the equivalent centrality points are adjusted according to the equation:

$$\langle p_{\mathrm{T}} \rangle = C\, N_{\mathrm{ch}}^{c_s^2}, \tag{15}$$

with c_s^2 as the free parameter. Here, C is a normalization constant that depends on the system volume and other proportionality factors.

In order to estimate c_s^2, the effective temperature of the system T_{eff} is assessed by using the relation

$$\langle p_{\mathrm{T}} \rangle \approx 3\, T_{\mathrm{eff}} \tag{16}$$

The values for the speed of sound are then plotted as a function of this effective temperature.

Using this mapping, each centrality bin is associated with a corresponding value of T_{eff}, enabling the study of the multiplicity dependence of $\langle p_{\mathrm{T}} \rangle$ in terms of an effective temperature scale. Under the assumption that the charged-particle multiplicity is proportional to the entropy of the system, and that the effective temperature extracted from $\langle p_{\mathrm{T}} \rangle$ reflects the average thermal scale, c_s^2 can be approximated experimentally by the logarithmic derivative in Equation 14.

The extraction of medium-related properties from experimental observables necessarily relies on reconstructed final-state particles within a finite kinematic acceptance [71]. In particular, the mean transverse momentum $\langle p_{\mathrm{T}} \rangle$ and any derived quantity such as the effective temperature T_{eff} or the speed of sound squared c_s^2 depend on the range of transverse momentum and pseudorapidity over which particles are selected.

In pPb collisions, this dependence is especially relevant due to the coexistence of multiple particle production mechanisms across different kinematic regimes [10]. Low–p_{T} particles are predominantly produced through soft processes and are expected to be sensitive to collective expansion, whereas high–p_{T} particles, in general, are from hard scatterings [72]. Similarly, the η acceptance determines the degree to which the measurement probes the midrapidity region, where particle production is more symmetric and collective effects are expected to be stronger [3]. For these reasons, it is interesting to study the stability of the observables used in this work under variations of the kinematic selection criteria.

In this analysis, several transverse momentum selections are considered besides the full inclusive range $p_{\mathrm{T}} > 0$ GeV, including higher p_{T} thresholds of $p_{\mathrm{T}} > 0.3$ GeV and $p_{\mathrm{T}} > 0.5$ GeV, as well as the addition of upper limits of $p_{\mathrm{T}} < 3$ GeV, $p_{\mathrm{T}} < 5$ GeV and $p_{\mathrm{T}} < 10$ GeV.

On the other hand, restricting the analysis to midrapidity (e.g., $\eta < 1.5$) minimizes the effect of other types of correlations (e.g., from hadronic jets) by enlarging the pseudorapidity gap between the regions used to determine the centrality classes and to measure charged particle multiplicity and transverse momentum [73, 74]. A stable behavior of the extracted observables under reasonable variations of the pseudorapidity acceptance provides further evidence that the measurement probes global properties of the system rather than kinematic effects.

The analysis was performed using CERN's ROOT software, and the framework applied in this work consisted in writing ROOT macros in order to correctly read, select, filter and analyze the data in order to calculate the final observables. All the ROOT macros used in this analysis were written in C++ and are available at `https://github.com/lucasdoriac/pPb_master_analysis/`.

4.6 Systematic uncertainties

Although no quantitative evaluation of systematic uncertainties is performed in this work, the dominant sources of systematic effects relevant to the analysis are discussed in a qualitative manner in order to assess their potential impact on the results. The discussion follows the standard approach adopted in CMS analyses of pPb collisions and reflects the main detector and analysis-related contributions that can affect the observables [75].

Systematic uncertainties associated with the trigger selection arise from the efficiency of the minimum-bias and high-multiplicity triggers and their dependence on event activity [9]. Uncertainties related to the reconstruction of the primary vertex affect both event-selection and track association. These uncertainties may arise from finite momentum resolution of the tracking system reconstruction resolution and from residual pileup contamination. Although pileup levels in pPb collisions are significantly lower than in pp collisions, the presence of multiple reconstructed vertices can still bias multiplicity-dependent measurements. Systematic effects are thus estimated by varying the vertex selection criteria or by comparing results obtained with stricter pileup rejection requirements [61].

Acceptance effects related to the finite pseudorapidity coverage of the tracker may also introduce systematic biases, especially in asymmetric collision systems such as pPb. These effects are usually studied by restricting the analysis to regions of uniform detector acceptance [60].

Finally, in CMS analyzes systematic uncertainties associated with the Hagedorn extrapolation are typically assessed by varying the fit range, modifying the functional form, and propagating the resulting variations to the final observables.

5 Results and insights

This Chapter presents the results for $c_s^2(T_{\text{eff}})$ obtained in this work using the methodology described in Chapter 4. Results for applying kinematic cuts on p_{T} and η are also presented.

Figure 23 presents the results for c_s^2 as a function of T_{eff} for pPb collisions at $\sqrt{s_{\text{NN}}} = 5.02$ TeV and $\sqrt{s_{\text{NN}}} = 8.16$ TeV in the pseudorapidity window $|\eta| < 1.5$ and extrapolation to $p_{\text{T}} > 0$ GeV. For the 30% most central events, the observed trend for $c_s^2(T_{\text{eff}})$ follows the trend from lattice QCD calculations. The results are also compared to predictions from the TRAJECTUM model [70] for $c_s^2(T_{\text{eff}})$, in order to discuss the possible creation of a medium in pPb collisions. The TRAJECTUM model is a computational framework designed to simulate the full evolution of the collisions, including the initial stages, a viscous hydrodynamic phase governed by transport coefficients, and a subsequent hadronic gas phase. The parameters of the TRAJECTUM model are constrained via a global Bayesian analysis of a wide range of experimental observables measured in heavy-ion collisions at the LHC. The quantitative results obtained for c_s^2 and T_{eff} are given in Table 4 of the Appendix A.

The results are also compared to predictions from the HIJING model [76] for $c_s^2(T_{\text{eff}})$, which serves as a scenario without the formation of a collectively expanding medium. HIJING is a Monte-Carlo (MC) event generator based on perturbative QCD for hard processes combined with phenomenological modeling of soft particle production. Comparisons with HIJING therefore allow one to assess whether the observed behavior of can be attributed to non-collective particle production mechanisms or whether it requires the presence of a medium with hydrodynamic-like properties.

For the 30–80% centrality bin, the calculation deviates strongly from both TRAJECTUM and HIJING predictions. It also deviates from the expected behaviour that c_s^2 monotonically increases with T_{eff} for values above $T_{\text{c}} \sim 155$ MeV. For the 30% most central events, data exhibits a smooth increase of c_s^2 with increasing T_{eff}. The HIJING results yield significantly smaller values of c_s^2 and also fail to reproduce the observed T_{eff} dependence, reflecting the absence of collective medium effects in the model. In contrast, the TRAJECTUM predictions exhibit a more qualitative agreement with the data, specially the trend for the 30% most central collisions.

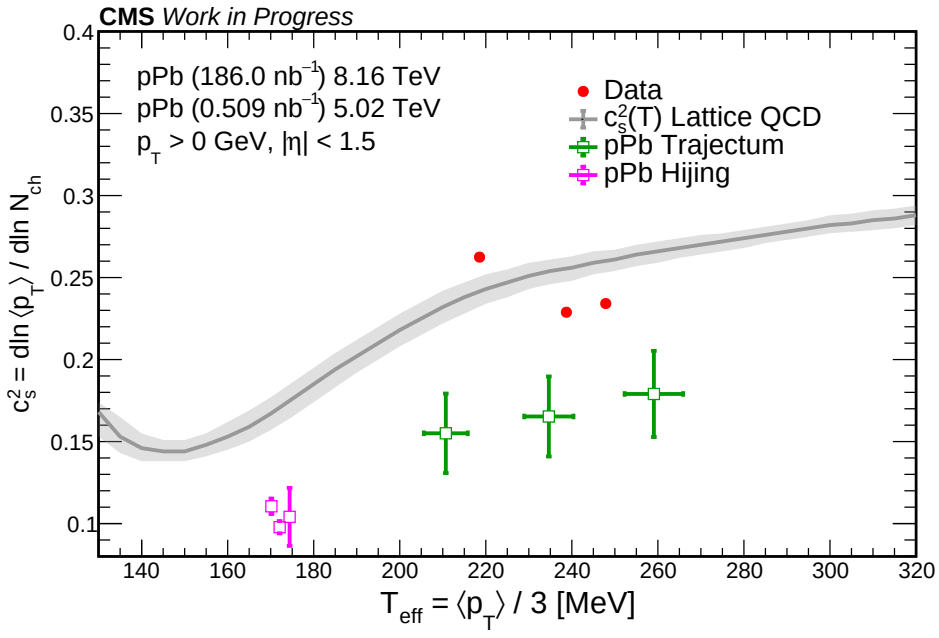


Figure 23 – Results for c_s^2 as a function of the effective temperature T_{eff} estimated using $T_{\text{eff}} \approx 0.33\,\langle p_{\text{T}}\rangle$. The HIJING event generator, which does not account for medium effects in the collision system, predicts values significantly inconsistent with the pPb data. For the 30% most central events, c_s^2 increases with the effective temperature T_{eff}. Only statistical uncertainties are shown and the error bars in data are smaller than the marker sizes.

An important result observed from Figure 23 is that the HIJING simulation, which does not incorporate thermodynamic and hydrodynamic effects, predicts values for $c_s^2(T_{\text{eff}})$ that are significantly inconsistent with the pPb data. This suggests that physical mechanisms governing bulk particle production in pPb collisions are absent in HIJING. On the other hand, the TRAJECTUM model shows closer results compared to the data.

A recent study by Gardim et. al [41] investigated the thermodynamic properties of matter formed in pPb collisions at $\sqrt{s_{NN}} = 5.02$ TeV using hydrodynamic simulations. Their results indicate that only the 30% most-central pPb events exhibit thermodynamic properties consistent with those of a deconfined QGP, reaching effective temperatures of approximately $T_{\text{eff}} \sim 220$ MeV. In contrast, lower-multiplicity events do not reproduce the expected QGP equation-of-state behavior. This is most interestingly observed in Figure 23 results, where only 30% most-central pPb events follow the expected trend for $c_s^2(T_{\text{eff}})$. This remarkable observation may suggest that, if QGP is formed in pPb collisions, it occurs only in the most central (highest-multiplicity) events, corresponding to an extremely small droplet whose volume is significantly smaller than that of central PbPb collisions, yet exhibiting comparable thermodynamic characteristics.

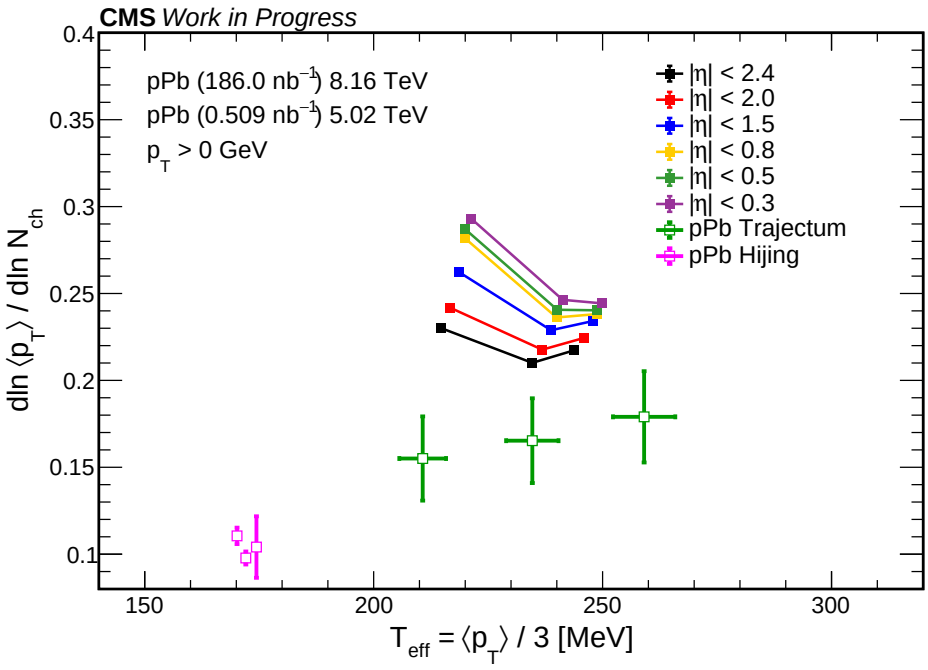


Figure 24 – Effect of pseudorapidity η acceptance variation on the extracted c_s^2 values for $p_{\mathrm{T}} > 0$ GeV.

Figures 24 and 25 show results for the kinematic cuts implemented in the calculation of $c_s^2(T_{\mathrm{eff}})$. The dependence of the extracted $c_s^2(T_{\mathrm{eff}})$ on the pseudorapidity acceptance is shown in Figure 24, where the analysis is repeated for several symmetric $|\eta|$ intervals ranging from $|\eta| < 0.3$ up to $|\eta| < 2.4$. The values of c_s^2 exhibit a weak dependence on the chosen η range, indicating that the observed behavior varies lightly in the analyzed pseudorapidity region. Additionally, a mild trend toward slightly larger values of c_s^2 for narrower η selections is visible. Comparison to HIJING predictions remain systematically below the measured values. This stability against variations in pseudorapidity acceptance supports the interpretation that the extracted $c_s^2(T_{\mathrm{eff}})$ reflects a genuine physical property of the system rather than an artifact of the detector coverage.

Figure 25 presents the dependence of $c_s^2(T_{\mathrm{eff}})$ on the transverse momentum selection of charged particles. The analysis is performed for different lower and upper p_{T} bounds, as indicated, including variations of the minimum p_{T} threshold and the maximum p_{T} included in the calculation. The extracted values of c_s^2 show sensitivity to the chosen p_{T} range, with lower c_s^2 values for lower thresholds on the transverse momenta. This behavior is consistent with expectations, as low–p_{T} particles are more sensitive to collective dynamics, while higher p_{T} contributions increasingly reflect hard processes. The TRAJECTUM model reproduces the qualitative dependence on the p_{T} selection, whereas HIJING still exhibits a

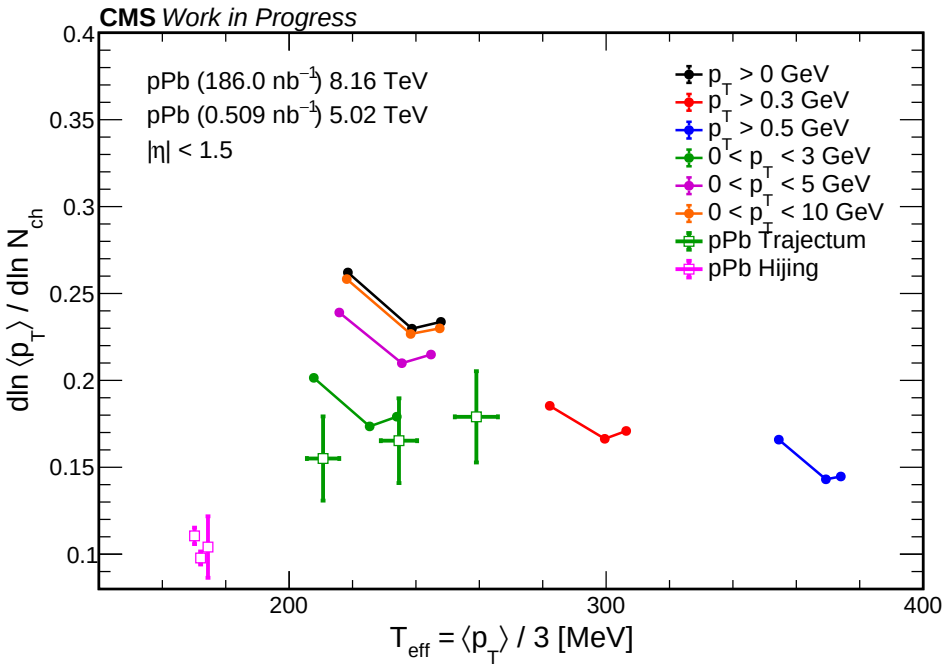


Figure 25 – Effect of transverse momentum p_{T} thresholds on the extracted c_s^2 values for $|\eta| < 1.5$. The cuts $p_{\mathrm{T}} > 0.3$ GeV and $p_{\mathrm{T}} > 0.5$ GeV strongly alter the general observed trend of $c_s^2(T_{\mathrm{eff}})$, expliciting the need for the extrapolation to $p_{\mathrm{T}} > 0$ GeV.

strong underestimation of the measured values. These observations are consistent with the fact that collective behaviour is predominantly present in the low–p_{T} sector. Moreover, the $p_{\mathrm{T}} > 0.3$ GeV and $p_{\mathrm{T}} > 0.5$ GeV cuts were not extrapolated to the $p_{\mathrm{T}} > 0$ GeV region. These cuts show increasingly disagreement with TRAJECTUM predictions and the trend observed by implying p_{T} upper limits. This indicates the necessity of using extrapolation methods for the $p_{\mathrm{T}} > 0$ GeV region like used in this work to correct for detector bias.

6 Conclusion

This dissertation investigated the method to extract the speed of sound squared c_s^2 using proton-lead (pPb) collisions at center-of-mass energies of $\sqrt{s_{NN}} = 5.02$ TeV and $\sqrt{s_{NN}} = 8.16$ TeV collected by the CMS experiment at the CERN-LHC. The analysis was a study of the correlation between the mean transverse momentum of charged particles, $\langle p_{\mathrm{T}} \rangle$, and the charged-particle multiplicity N_{ch}, which provides access to the thermodynamic properties of the system through the relation $d\ln\langle p_T \rangle / d\ln N_{\mathrm{ch}}$ and the observed proportion between $\langle p_{\mathrm{T}} \rangle$ and T_{eff}.

The collision data analysis was described in Chapter 4, including event and track selection, quality assurance studies, centrality estimation and the classification of events into multiplicity classes. The transverse momentum spectra of charged particles were fitted and extrapolated to the low-p_{T} region in order to obtain a consistent determination of $\langle p_T \rangle$ across all event classes and minimize fluctuations. An effective temperature T_{eff} was defined based on the mean transverse momentum, allowing the extraction of $c_s^2(T_{\mathrm{eff}})$. Variations in the kinematic selections of transverse momentum and pseudorapidity were studied to observe effects and possible trends in the calculated $c_s^2(T_{\mathrm{eff}})$.

The results presented in Chapter 5 show that the extracted values of c_s^2 exhibit a strong disagreement with HIJING predictions for the same collision energy and event activity. For the 30% most central events, $c_s^2(T_{\mathrm{eff}})$ increases with the effective temperature, as expected. Compared to TRAJECTUM results, the values of c_s^2 are found to be systematically higher than those predicted by the hydrodynamic model tuned to heavy-ion collisions.

A moderate sensitivity to the transverse momentum range is observed, with smaller values of $c_s^2(T_{\mathrm{eff}})$ obtained when restricting the analysis to low–p_{T} particles, consistent with the expectation that collective effects predominantly affect the soft sector. Additionally, the consideration of $p_{\mathrm{T}} > 0.3$ GeV distributions show that the extrapolation to p_{T} GeV is needed to correct for detector bias.

Future measurements with different collision energies, extended precision and improved modeling of initial-state effects will be essential to further clarify the nature of collectivity in small systems. In particular, comparisons across pp, pPb, OO, NeNe and PbPb collisions using unified analysis techniques may provide deeper insight into the QGP-like behavior in these collisions.

Bibliography

[1] A. Bazavov et al. “Equation of state in (2+1)-flavor QCD”. In: *Phys. Rev. D* 90 (2014), p. 094503.

[2] S. Borsányi et al. “Full result for the QCD equation of state with (2+1) flavors”. In: *Physics Letters B* 730 (Mar. 2014), pp. 99–104. ISSN: 0370-2693. DOI: 10.1016/j.physletb.2014.01.007. URL: http://dx.doi.org/10.1016/j.physletb.2014.01.007.

[3] W. Busza, K. Rajagopal, and W. van der Schee. “Heavy Ion Collisions: The Big Picture and the Big Questions”. In: *Annual Review of Nuclear and Particle Science* 68.1 (Oct. 2018), pp. 339–376. ISSN: 1545-4134. DOI: 10.1146/annurev-nucl-101917-020852. URL: http://dx.doi.org/10.1146/annurev-nucl-101917-020852.

[4] M. G. Alford et al. “Color superconductivity in dense quark matter”. In: *Reviews of Modern Physics* 80.4 (Nov. 2008), pp. 1455–1515. ISSN: 1539-0756. DOI: 10.1103/revmodphys.80.1455. URL: http://dx.doi.org/10.1103/RevModPhys.80.1455.

[5] J. D. Bjorken. “Highly relativistic nucleus-nucleus collisions: The central rapidity region”. In: *Phys. Rev. D* 27 (1 Jan. 1983), pp. 140–151. DOI: 10.1103/PhysRevD.27.140. URL: https://link.aps.org/doi/10.1103/PhysRevD.27.140.

[6] U. Heinz and R. Snellings. “Collective Flow and Viscosity in Relativistic Heavy-Ion Collisions”. In: *Annual Review of Nuclear and Particle Science* 63.1 (Oct. 2013), pp. 123–151. ISSN: 1545-4134. DOI: 10.1146/annurev-nucl-102212-170540. URL: http://dx.doi.org/10.1146/annurev-nucl-102212-170540.

[7] F. G. Gardim et al. “Thermodynamics of hot strong-interaction matter from ultra-relativistic nuclear collisions”. In: *Nature Physics* 16.6 (Mar. 2020), pp. 615–619. ISSN: 1745-2481. DOI: 10.1038/s41567-020-0846-4. URL: http://dx.doi.org/10.1038/s41567-020-0846-4.

[8] F. G. Gardim, A. V. Giannini, and J.-Y. Ollitrault. “Accessing the speed of sound in relativistic ultracentral nucleus-nucleus collisions using the mean transverse momentum”. In: *Physics Letters B* 856 (Sept. 2024), p. 138937. ISSN: 0370-2693.

DOI: 10.1016/j.physletb.2024.138937. URL: http://dx.doi.org/10.1016/j.physletb.2024.138937.

[9] CMS Collaboration. "Observation of long-range, near-side angular correlations in pPb collisions at the LHC". In: *Physics Letters B* 718.3 (Jan. 2013), pp. 795–814. ISSN: 0370-2693. DOI: 10.1016/j.physletb.2012.11.025. URL: http://dx.doi.org/10.1016/j.physletb.2012.11.025.

[10] K. Dusling, W. Li, and B. Schenke. "Novel collective phenomena in high-energy proton–proton and proton–nucleus collisions". In: *International Journal of Modern Physics E* 25.01 (Jan. 2016), p. 1630002. ISSN: 1793-6608. DOI: 10.1142/s0218301316300022. URL: http://dx.doi.org/10.1142/S0218301316300022.

[11] J. L. Nagle and W. A. Zajc. "Small System Collectivity in Relativistic Hadronic and Nuclear Collisions". In: *Annual Review of Nuclear and Particle Science* 68.1 (Oct. 2018), pp. 211–235. ISSN: 1545-4134. DOI: 10.1146/annurev-nucl-101916-123209. URL: http://dx.doi.org/10.1146/annurev-nucl-101916-123209.

[12] D. J. Griffiths. *Introduction to Elementary Particles*. 1987. ISBN: 978-0-471-60386-3, 978-3-527-61846-0. DOI: 10.1002/9783527618460.

[13] G. Chachamis. *Phenomenology of the Strong Interaction*. Lecture notes, 9th Mini-School on Particle and Astroparticle Physics. Oeiras, Portugal, Feb. 2024.

[14] M. Gell-Mann. "The Eightfold Way: A Theory of strong interaction symmetry". In: (Mar. 1961). DOI: 10.2172/4008239.

[15] G. Zweig. "Memories of Murray and the Quark Model". In: *International Journal of Modern Physics A* 25.20 (Aug. 2010), pp. 3863–3877. ISSN: 1793-656X. DOI: 10.1142/s0217751x10050494. URL: http://dx.doi.org/10.1142/S0217751X10050494.

[16] G. 't Hooft and M. J. G. Veltman. "Regularization and Renormalization of Gauge Fields". In: *Nucl. Phys. B* 44 (1972), pp. 189–213. DOI: 10.1016/0550-3213(72)90279-9.

[17] D. J. Gross and F. Wilczek. "Ultraviolet Behavior of Non-Abelian Gauge Theories". In: *Phys. Rev. Lett.* 30 (26 June 1973), pp. 1343–1346. DOI: 10.1103/PhysRevLett.30.1343. URL: https://link.aps.org/doi/10.1103/PhysRevLett.30.1343.

[18] H. D. Politzer. "Reliable Perturbative Results for Strong Interactions?" In: *Phys. Rev. Lett.* 30 (26 June 1973), pp. 1346–1349. DOI: 10.1103/PhysRevLett.30.1346. URL: https://link.aps.org/doi/10.1103/PhysRevLett.30.1346.

[19] STAR Collaboration. *An Experimental Exploration of the QCD Phase Diagram: The Search for the Critical Point and the Onset of De-confinement*. 2010. arXiv: 1007.2613 [nucl-ex]. URL: https://arxiv.org/abs/1007.2613.

[20] W. Florkowski. *Phenomenology of Ultra-Relativistic Heavy-Ion Collisions*. Mar. 2010. ISBN: 978-981-4280-66-2.

[21] PHOBOS Collaboration. "The PHOBOS perspective on discoveries at RHIC". In: *Nucl. Phys. A* 757 (2005), pp. 28–101. DOI: 10.1016/j.nuclphysa.2005.03.084. arXiv: nucl-ex/0410022.

[22] W. Florkowski. *Ultra-relativistic heavy-ion collisions*. Lecture slides, 48th Karpacz Winter School of Theoretical Physics, CERN Indico. Available at: https://indico.cern.ch/event/186765/contributions/1458861/attachments/259542/362530/4_hic.pdf. Feb. 2012.

[23] J. Rafelski and B. Müller. "Strangeness Production in the Quark-Gluon Plasma". In: *Phys. Rev. Lett.* 48 (16 Apr. 1982), pp. 1066–1069. DOI: 10.1103/PhysRevLett.48.1066. URL: https://link.aps.org/doi/10.1103/PhysRevLett.48.1066.

[24] STAR Collaboration. "Experimental and theoretical challenges in the search for the quark–gluon plasma: The STAR Collaboration's critical assessment of the evidence from RHIC collisions". In: *Nucl. Phys. A* 757 (2005), pp. 102–183.

[25] A. Jaiswal and V. Roy. "Relativistic hydrodynamics in heavy-ion collisions". In: *Adv. High Energy Phys.* 2016 (2016), p. 9623034.

[26] J.-Y. Ollitrault. "Relativistic hydrodynamics for heavy-ion collisions". In: *Nuclear Physics A* 638 (1998), pp. 195c–206c. DOI: 10.1016/S0375-9474(98)00330-1.

[27] S. Schlichting and D. Teaney. "The First fm/c of Heavy-Ion Collisions". In: *Annual Review of Nuclear and Particle Science* 69.1 (Oct. 2019), pp. 447–476. ISSN: 1545-4134. DOI: 10.1146/annurev-nucl-101918-023825. URL: http://dx.doi.org/10.1146/annurev-nucl-101918-023825.

[28] ALICE Collaboration. "Charged-Particle Multiplicity Density at Midrapidity in Central Pb-Pb Collisions at $\sqrt{s_{NN}} = 2.76$ TeV". In: *Phys. Rev. Lett.* 105 (25 Dec. 2010), p. 252301. DOI: 10.1103/PhysRevLett.105.252301. URL: https://link.aps.org/doi/10.1103/PhysRevLett.105.252301.

[29] F. Karsch. "Lattice QCD at high temperature and density". In: *Lect. Notes Phys.* 583 (2002), pp. 209–249. DOI: 10.1007/3-540-45792-5_6.

[30] CMS Collaboration. "Charged-particle angular correlations in XeXe collisions at $\sqrt{s_{NN}} = 5.44$ TeV". In: *Physical Review C* 100.4 (2019), p. 044902. DOI: 10.1103/PhysRevC.100.044902.

[31] ALICE Collaboration. "Elliptic flow of charged particles in Pb–Pb collisions at $\sqrt{s_{NN}} = 2.76$ TeV". In: *Phys. Rev. Lett.* 105 (2010), p. 252302. DOI: 10.1103/PhysRevLett.105.252302.

[32] L. Van Hove. "Multiplicity dependence of pt spectrum as a possible signal for a phase transition in hadronic collisions". In: *Physics Letters B* 118.1 (1982), pp. 138–140. ISSN: 0370-2693. DOI: https://doi.org/10.1016/0370-2693(82)90617-7. URL: https://www.sciencedirect.com/science/article/pii/0370269382906177.

[33] ALICE Collaboration. "Centrality dependence of π, K, and p production in Pb–Pb collisions at $\sqrt{s_{NN}} = 2.76$ TeV". In: *Phys. Rev. C* 88 (2013), p. 044910. DOI: 10.1103/PhysRevC.88.044910.

[34] P. Romatschke and U. Romatschke. "Relativistic Fluid Dynamics In and Out of Equilibrium: Ten Years of Progress in Theory and Numerical Simulations of Nuclear Collisions". In: (2017). arXiv:1712.05815 [nucl-th]. arXiv: 1712.05815 [nucl-th].

[35] P. F. Kolb and U. Heinz. "Hydrodynamic description of ultrarelativistic heavy-ion collisions". In: *nucl-th/0305084* (2003).

[36] A. Jaiswal and V. Roy. "Relativistic Hydrodynamics in Heavy-Ion Collisions: General Aspects and Recent Developments". In: *Advances in High Energy Physics* 2016 (Jan. 2016), pp. 1–39. DOI: 10.1155/2016/9623034.

[37] O. Philipsen. "The QCD equation of state from the lattice". In: *Prog. Part. Nucl. Phys.* 70 (2013), pp. 55–107. DOI: 10.1016/j.ppnp.2012.09.003.

[38] R. K. Pathria and P. D. Beale. *Statistical Mechanics*. 3rd ed. Elsevier, 2011. ISBN: 9780123821881.

[39] ALICE Collaboration. "Centrality determination of Pb-Pb collisions at $\sqrt{s_{NN}} = 2.76$ TeV with ALICE". In: *Phys. Rev. C* 88 (4 Oct. 2013), p. 044909. DOI: 10.1103/PhysRevC.88.044909. URL: https://link.aps.org/doi/10.1103/PhysRevC.88.044909.

[40] CMS Collaboration. "Centrality and pseudorapidity dependence of the transverse energy density in pPb collisions at $\sqrt{s_{\mathrm{NN}}} = 5.02, \mathrm{TeV}$". In: *Physical Review C* 100.2 (2019). CMS-HIN-14-014, p. 024902. DOI: 10.1103/PhysRevC.100.024902. arXiv: 1810.05745 [hep-ex].

[41] F. G. Gardim, R. Krupczak, and T. N. da Silva. "Smallest drop of QGP: Thermodynamic properties of p-Pb collisions". In: *Phys. Rev. C* 109 (1 Jan. 2024), p. 014904. DOI: 10.1103/PhysRevC.109.014904. URL: https://link.aps.org/doi/10.1103/PhysRevC.109.014904.

[42] O. S. Brüning et al. *LHC Design Report*. CERN Yellow Reports: Monographs. Geneva: CERN, 2004. DOI: 10.5170/CERN-2004-003-V-1. URL: https://cds.cern.ch/record/782076.

[43] S. N. et al. (Particle Data Group). "Review of Particle Physics". In: *Phys. Rev. D* 110 (3 Aug. 2024), p. 030001. DOI: 10.1103/PhysRevD.110.030001. URL: https://link.aps.org/doi/10.1103/PhysRevD.110.030001.

[44] CERN Education, Communications and Outreach Group. *LHC: the guide*. https://cds.cern.ch/record/2255762/files/CERN-Brochure-2017-002-Eng.pdf. Accessed 2025-11-28. 2017.

[45] L. Evans and P. Bryant. "LHC Machine". In: *Journal of Instrumentation* 3.08 (Aug. 2008), S08001. DOI: 10.1088/1748-0221/3/08/S08001. URL: https://doi.org/10.1088/1748-0221/3/08/S08001.

[46] W. Herr and B. Muratori. "Concept of luminosity". In: *CERN Accelerator School and DESY Zeuthen: Accelerator Physics*. Sept. 2003, pp. 361–377.

[47] S. I. Stone and L. Rosenberg. *Introduction to experimental particle physics*. Accessible via INSPIRE-HEP. World Scientific, 2019. ISBN: 978-981-12-4286-1. URL: https://inspirehep.net/files/fb324a45653a41cbe65af02c531cc401.

[48] A. Dainese et al. "INFN What Next: Ultra-relativistic Heavy-Ion Collisions". In: (Feb. 2016). DOI: 10.48550/arXiv.1602.04120.

[49] CMS Collaboration. "The CMS experiment at the CERN LHC". In: *Journal of Instrumentation* 3.08 (Aug. 2008), S08004. DOI: 10.1088/1748-0221/3/08/S08004. URL: https://dx.doi.org/10.1088/1748-0221/3/08/S08004.

[50] ATLAS Collaboration. "Observation of a new particle in the search for the Standard Model Higgs boson with the ATLAS detector at the LHC". In: *Physics Letters B* 716.1 (Sept. 2012), pp. 1–29. ISSN: 0370-2693. DOI: 10.1016/j.physletb.2012.08.020. URL: http://dx.doi.org/10.1016/j.physletb.2012.08.020.

[51] CMS Collaboration. "Observation of a new boson at a mass of 125 GeV with the CMS experiment at the LHC". In: *Physics Letters B* 716.1 (Sept. 2012), pp. 30–61. ISSN: 0370-2693. DOI: 10.1016/j.physletb.2012.08.021. URL: http://dx.doi.org/10.1016/j.physletb.2012.08.021.

[52] CMS Collaboration. "High-precision measurement of the W boson mass with the CMS experiment at the LHC". In: (2024). arXiv: 2412.13872 [hep-ex]. URL: https://arxiv.org/abs/2412.13872.

[53] CMS Collaboration. "Overview of high-density QCD studies with the CMS experiment at the LHC". In: *Physics Reports* 1115 (2025). CMS physics results from the first decade of LHC data, pp. 219–367. ISSN: 0370-1573. DOI: https://doi.org/10.1016/j.physrep.2024.11.007. URL: https://www.sciencedirect.com/science/article/pii/S0370157324004046.

[54] C. A. Bernardes. *Extracting the speed of sound in the strongly interacting matter created in relativistic nuclear collisions with the CMS experiment*. 2024. arXiv: 2312.11758 [nucl-ex]. URL: https://arxiv.org/abs/2312.11758.

[55] CERN AC. "Layout of CMS". 1998. URL: https://cds.cern.ch/record/39040.

[56] CMS Collaboration. "Description and performance of track and primary-vertex reconstruction with the CMS tracker". In: *Journal of Instrumentation* 9.10 (2014). CMS-DP-2014-027 / CMS Tracker Performance paper, P10009. DOI: 10.1088/1748-0221/9/10/P10009. arXiv: 1405.6569 [physics.ins-det].

[57] B. Vormwald. "The CMS inner tracker – transition from LHC Run I to Run II and first experience of Run II". In: Mar. 2016, p. 229. DOI: 10.22323/1.234.0229.

[58] D. Barney. "CMS Detector Slice". CMS Collection. 2016. URL: https://cds.cern.ch/record/2120661.

[59] I. Neutelings. *CMS coordinate system*. https://tikz.net/axis3d_cms/. Accessed: 2025-08-12. 2017.

[60] CMS Collaboration. "The CMS trigger system". In: *Journal of Instrumentation* 12.01 (Jan. 2017), P01020–P01020. ISSN: 1748-0221. DOI: 10.1088/1748-0221/12/01/p01020. URL: http://dx.doi.org/10.1088/1748-0221/12/01/P01020.

[61] L. Viliani. "CMS tracker performance and readiness for LHC Run II". In: *Nuclear Instruments and Methods in Physics Research Section A: Accelerators, Spectrometers, Detectors and Associated Equipment* 824 (2016). Frontier Detectors for Frontier Physics: Proceedings of the 13th Pisa Meeting on Advanced Detectors, pp. 67–69. ISSN: 0168-9002. DOI: https://doi.org/10.1016/j.nima.2015.09.046. URL: https://www.sciencedirect.com/science/article/pii/S0168900215011018.

[62] CMS Collaboration. *Study of χ_c production in pPb collisions at $\sqrt{s_{NN}} = 8.16$ TeV with the CMS experiment*. CMS Physics Analysis Summary CMS-PAS-HIN-22-003. CERN, available at https://cds.cern.ch/record/2930770/files/HIN-22-003-pas.pdf. 2025.

[63] R. Brun and F. Rademakers. "ROOT — An object oriented data analysis framework". In: *Nuclear Instruments and Methods in Physics Research Section A* 389 (1997), pp. 81–86. DOI: 10.1016/S0168-9002(97)00048-X.

[64] M. L. Miller et al. "Glauber Modeling in High-Energy Nuclear Collisions". In: *Annual Review of Nuclear and Particle Science* 57 (2007), pp. 205–243. DOI: 10.1146/annurev.nucl.57.090506.123020.

[65] J. L. Albacete et al. "Predictions for p+Pb collisions at $\sqrt{s_{NN}} = 5$ TeV". In: *International Journal of Modern Physics E* 22.04 (2013), p. 1330007. DOI: 10.1142/S0218301313300075.

[66] C. Loizides. "Glauber modeling of high-energy nuclear collisions at the LHC". In: *Nuclear Physics A* 956 (2016), pp. 200–207. DOI: 10.1016/j.nuclphysa.2016.03.047.

[67] C. Tsallis. "Possible generalization of Boltzmann–Gibbs statistics". In: *Journal of Statistical Physics* 52 (1988), pp. 479–487. DOI: 10.1007/BF01016429.

[68] CMS Collaboration. "Transverse momentum spectra of charged particles in pp collisions at $\sqrt{s} = 0.9$ and 7 TeV". In: *Journal of High Energy Physics* 02 (2010), p. 041. DOI: 10.1007/JHEP02(2010)041. arXiv: 1002.0621 [hep-ex].

[69] P. D. Group. "Review of Particle Physics". In: *Progress of Theoretical and Experimental Physics* (2024).

[70] G. Nijs and W. van der Schee. "Predictions and postdictions for relativistic lead and oxygen collisions with the computational simulation code Trajectum". In: *Phys. Rev. C* 106.4 (2022), p. 044903. DOI: 10.1103/PhysRevC.106.044903. arXiv: 2110.13153 [nucl-th].

[71] P. Braun-Munzinger et al. "Properties of hot and dense matter from relativistic heavy ion collisions". In: *Physics Reports* 621 (Mar. 2016), pp. 76–126. ISSN: 0370-1573. DOI: 10.1016/j.physrep.2015.12.003. URL: http://dx.doi.org/10.1016/j.physrep.2015.12.003.

[72] R. J. Fries et al. "Hadronization in Heavy-Ion Collisions: Recombination and Fragmentation of Partons". In: *Phys. Rev. Lett.* 90 (20 May 2003), p. 202303. DOI: 10.1103/PhysRevLett.90.202303. URL: https://link.aps.org/doi/10.1103/PhysRevLett.90.202303.

[73] CMS Collaboration. "Observation of long-range near-side angular correlations in proton–lead collisions at the LHC". In: *Physics Letters B* 718 (2013), pp. 795–814. DOI: 10.1016/j.physletb.2012.11.025. arXiv: 1210.5482 [nucl-ex].

[74] ALICE Collaboration. "Long-range angular correlations on the near and away side in p–Pb collisions at $\sqrt{s_{NN}} = 5.02$ TeV". In: *Physics Letters B* 719 (2013), pp. 29–41. DOI: 10.1016/j.physletb.2013.01.012. arXiv: 1212.2001 [nucl-ex].

[75] CMS Collaboration. "Pseudorapidity distribution of charged hadrons in proton–proton collisions at $\sqrt{s} = 13TeV$". In: *Physics Letters B* 751 (Dec. 2015), pp. 143–163. ISSN: 0370-2693. DOI: 10.1016/j.physletb.2015.10.004. URL: http://dx.doi.org/10.1016/j.physletb.2015.10.004.

[76] M. Gyulassy and X.-N. Wang. "HIJING 1.0: A Monte Carlo program for parton and particle production in high-energy hadronic and nuclear collisions". In: *Comput. Phys. Commun.* 83 (1994), p. 307. DOI: 10.1016/0010-4655(94)90057-4. arXiv: nucl-th/9502021.

APPENDIX A – Numerical results

Table 2 – Charged-particle multiplicity N_{ch} and mean transverse momentum $\langle p_{\mathrm{T}} \rangle$ on the pseudorapidity interval $|\eta| < 1.5$ for pPb collisions at $\sqrt{s_{NN}} = 5.02$ TeV. An extrapolation using a Hagedorn function was performed to the $p_{\mathrm{T}} < 0.3$ GeV region. The centrality classes correspond to 30–80%, 1–30%, and 0–1%, respectively. Statistical uncertainties were calculated only.

Centrality	N_{ch}	Stat. Unc.	$\langle p_{\mathrm{T}} \rangle$ [GeV]	Stat. Unc.
30–80%	40.2791	0.0018	0.644556	2.64×10^{-5}
1–30%	85.4897	0.0036	0.701648	2.69×10^{-5}
0–1%	146.213	0.0077	0.727440	3.44×10^{-5}

Table 3 – Charged-particle multiplicity N_{ch} and mean transverse momentum $\langle p_{\mathrm{T}} \rangle$ on the pseudorapidity interval $|\eta| < 1.5$ for pPb collisions at $\sqrt{s_{NN}} = 8.16$ TeV. An extrapolation using a Hagedorn function was performed to the $p_{\mathrm{T}} < 0.3$ GeV region. The centrality classes correspond to 30–80%, 1–30%, and 0–1%, respectively. Statistical uncertainties were calculated only.

Centrality	N_{ch}	Stat. Unc.	$\langle p_{\mathrm{T}} \rangle$ [GeV]	Stat. Unc.
30–80%	45.8172	0.0019	0.666721	2.69×10^{-5}
1–30%	102.108	0.0041	0.730759	2.75×10^{-5}
0–1%	176.132	0.0070	0.759852	2.77×10^{-5}

Table 4 – Effective temperature T_{eff} and squared speed of sound c_s^2 for different centrality classes calculated using Equations 15 and 16, respectively. Statistical uncertainties were calculated only.

Centrality	c_s^2	Stat. Unc.	T_{eff} [MeV]	Stat. Unc. [MeV]
30–80%	0.262456	4.49×10^{-4}	218.54	0.0063
1–30%	0.228853	3.03×10^{-4}	238.73	0.0064
0–1%	0.234146	3.22×10^{-4}	247.88	0.0074